

Revisiting the Group-Dominant Elliptical NGC 5044 in the Radio Band: Continuum Emission and Detection of HI Absorption

KAMLESH RAJPUROHIT,¹ TIRNA DEB,¹ KONSTANTINOS KOLOKYTHAS,^{2,3} KSHITIJ THORAT,⁴ EWAN O’ SULLIVAN,¹ GERRIT SCHELLENBERGER,¹ LAURENCE P. DAVID,¹ JAN M. VRTILEK,¹ SIMONA GIACINTUCCI,⁵ WILLIAM FORMAN,¹ CHRISTINE JONES,¹ AND MPATI RAMATSOKU^{6,2,3}

¹*Center for Astrophysics | Harvard & Smithsonian, 60 Garden Street, Cambridge, MA 02138, USA*

²*Centre for Radio Astronomy Techniques and Technologies, Department of Physics and Electronics, Rhodes University, P.O. Box 94, Makhanda 6140, South Africa*

³*South African Radio Astronomy Observatory, 2 Fir Street, Observatory 7925, South Africa*

⁴*Department of Physics, University of Pretoria, Hatfield, Pretoria 0028, South Africa*

⁵*Naval Research Laboratory, 4555 Overlook Avenue SW, Code 7213, Washington, DC 20375, US*

⁶*INAF-Cagliari Astronomical Observatory, Via della Scienza 5, I-09047 Selargius (CA), Italy*

ABSTRACT

We present new MeerKAT L-band (continuum and H I) and upgraded Giant Metrewave Radio Telescope (300-850 MHz) observations of the archetypal cool-core group-dominant early-type galaxy NGC 5044. Our new continuum images reveal diffuse, steep spectrum ($\alpha_{0.99\text{ GHz}}^{1.56\text{ GHz}} = -1.53 \pm 0.6$) radio emission extending about 25 kpc around the unresolved radio core. The observed radio emission overlaps the known X-ray cavities, but is not confined to them. We also find the first direct evidence of neutral atomic gas in NGC 5044, in the form of a 3.8σ significant two-component H I absorption line seen against the emission of the active nucleus. The peak velocities are well correlated with the previously reported CO(2-1) absorption, but the H I lines are moderately broader, spanning velocities from 265 km s^{-1} to 305 km s^{-1} . We do not detect H I emission, but place an upper limit of $M_{\text{HI}} < 5.4 \times 10^7 M_{\odot}$ in the central $15''$ (2.2 kpc) of the galaxy. This is significantly less than the estimated molecular gas content, and implies a molecular-to-atomic mass ratio of $\gtrsim 1.7:1$, consistent with these gas phases forming through cooling from the hot intra-group medium. We also constrain the spin temperature to $T_{\text{spin}} \leq 950 \text{ K}$, indicating that the detected H I is in the cold neutral phase.

Keywords: Galaxy groups; Early-type galaxies; Cooling flows; Neutral hydrogen clouds

1. INTRODUCTION

It is now well established that heating by active galactic nuclei (AGNs) plays an important role in balancing radiative cooling in the hot atmospheres of elliptical galaxies, galaxy groups, and clusters. Cooling appears to be regulated by a feedback loop, in which cooled gas fuels the AGN, triggering the launch of relativistic jets which heat and mix the surrounding medium via a variety of mechanisms (e.g., shocks, sound waves, turbulence, uplift), thereby suppressing the cooling (see, e.g., Churazov et al. 2001, 2002 and reviews by Fabian 2012; McNamara & Nulsen 2012; Gitti et al. 2012; Gaspari et al. 2020; Donahue & Voit 2022). Our understanding of AGN feedback is anchored by multi-

frequency observations: in the radio continuum to trace the relativistic jets and the lobes they inflate (e.g., Birzan et al. 2008; Giacintucci et al. 2011; Birzan et al. 2020; Pasini et al. 2021, 2022); in the X-ray to measure the thermodynamic state of the hot medium and see the impact of the jets via cavities, shock fronts, and uplifted material (e.g., Churazov et al. 2000; Dong et al. 2010; Kirkpatrick et al. 2011; Randall et al. 2015; Russell et al. 2019; Ubertosi et al. 2023; Plšek et al. 2024); and via emission and absorption line observations (most commonly CO and H α) which trace the gas which cools out of the hot phase and forms the reservoir of fuel on which the AGN draws (e.g., Edge 2001; Salomé & Combes 2003; Hogan 2014; Pulido et al. 2018; Lakhchaura et al. 2018; Olivares et al. 2019, 2022).

Galaxy groups are perhaps the most interesting mass scale ($\sim 10^{13}$ - $10^{14} M_{\odot}$) for studies of the cooling/AGN feedback cycle. At the typical $\sim 1 \text{ keV}$ temperatures of the intra-group medium (IGrM), line emission makes radiative cooling more

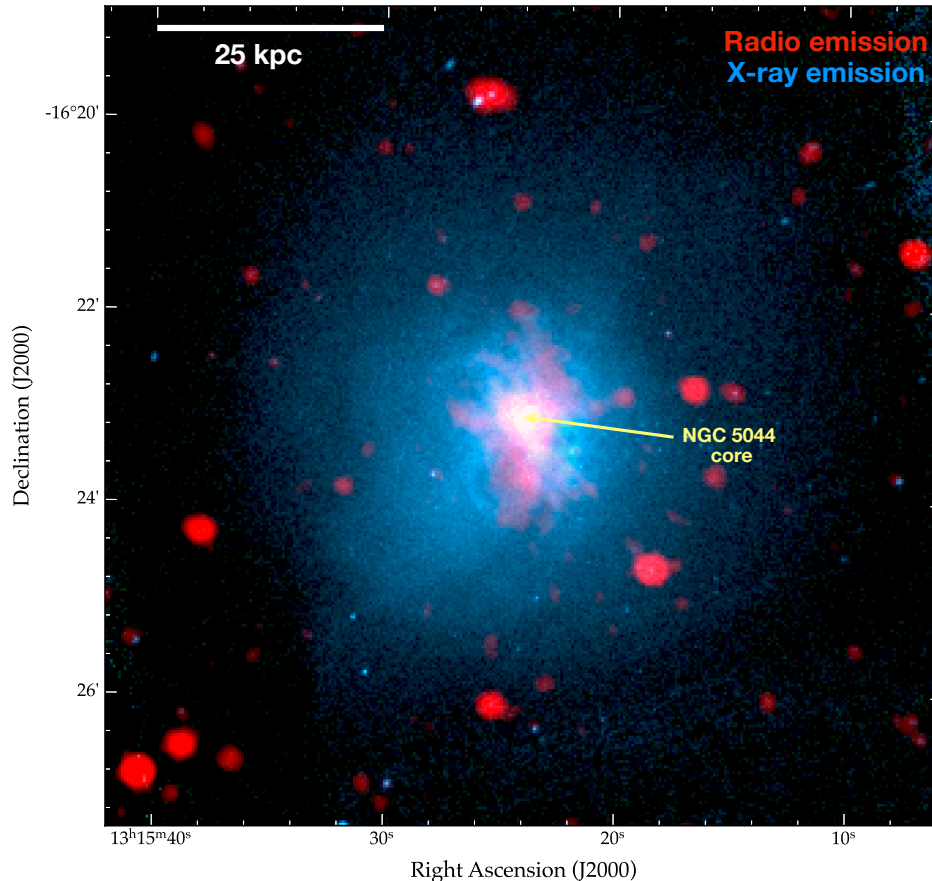


Figure 1. Radio and X-ray overlay of NGC 5044. The intensity in red shows the radio emission observed with uGMRT at a central frequency of 380 MHz ($10''$ resolution). The intensity in blue shows *Chandra* X-ray emission in the 0.5 – 2.0 keV band.

efficient than in clusters, leading to the finding that there are essentially no non-cool-core groups by the standards applied to clusters (O’Sullivan et al. 2017). It has also been shown that, while in clusters the gravitational binding energy of the ICM greatly exceeds the total energy available from the supermassive black holes (SMBHs) of cluster-dominant galaxies, in groups the two energies are comparable (Eckert et al. 2021). AGN feedback therefore has a much greater potential to affect the IGrM, possibly even to the point of driving gas out of the group. This is the most likely explanation for the reduced gas fractions observed in galaxy groups (Gastaldello et al. 2007; Lovisari et al. 2015; Eckert et al. 2016). Over the history of these systems, AGN feedback has heated the IGrM and driven gas out to large radii. Groups are thus a critically important environment for feedback studies, with the majority of systems likely affected by their AGN, and the feedback loop requires a fine balance to avoid expelling the IGrM.

The NGC 5044 group is the archetypal AGN feedback system for the group mass scale, with an exceptional multiwavelength observational dataset providing insight into its history and current state. X-ray observations reveal the nested cold fronts characteristic of sloshing, likely caused by the recent passage of a massive spiral galaxy through the

system (Buote et al. 2003; Gastaldello et al. 2009; David et al. 2009; Gastaldello et al. 2013; O’Sullivan et al. 2014). Nonetheless, the IGrM is highly centrally concentrated, with a steeply declining central temperature profile, short central cooling times, and low central entropy, indicating rapid cooling (David et al. 1994, 2011). The IGrM core contains a complex collection of cavities and cooling filaments (see Figure 1; David et al. 2017). The warm and cold phases of the cooling flow are observed in the form of an extended filamentary $H\alpha$ nebula (David et al. 2014) and molecular gas clouds traced by CO, [C II], and rovibrational H_2 line emission, with CO, HCN and HCO^+ also seen in absorption against the AGN (Kaneda et al. 2008; David et al. 2014; Werner et al. 2014; Temi et al. 2018; Schellenberger et al. 2020; Rose et al. 2019, 2023, 2024). The total molecular gas mass in the central $15''$ (2.3 kpc) of the galaxy is estimated to be $\sim 10^8 M_\odot$, one of the largest molecular reservoirs of any X-ray luminous group (Schellenberger et al. 2020).

A combination of X-ray and radio data provides evidence of at least three cycles of feedback from the AGN of NGC 5044 (Schellenberger et al. 2021). Deep *Chandra* imaging shows a pair of cavities on ~ 5 kpc scales, as well as a second, younger pair on sub-kiloparsec scales in the

galaxy nucleus (David et al. 2017). Very Long Baseline Array observations in C and X-band (5 and 8.5 GHz respectively) show even younger parsec-scale jets (Schellenberger et al. 2021). Interestingly, these jets are oriented roughly northeast-southwest, orthogonal to the orientation of the cavities.

On larger scales, radio observations have presented conflicting views of the AGN activity. Grossová et al. (2022) analyzed Very Large Array (VLA) L-band (1.4 GHz) radio observations, with A configuration data showed hints of kiloparsec-scale jets aligned northeast-southwest, while lower resolution AnB configuration data showing possible ~ 4 kpc scale jets on an east-west axis. Giant Metrewave Radio Telescope (GMRT) 610 MHz data showed a possible small radio lobe extending ~ 12 kpc southeast of the core, possibly correlated with an X-ray filament but not with the X-ray cavities (Giacintucci et al. 2011). At the lowest frequency and largest scale, a GMRT 235 MHz observation showed what appeared to be a detached radio lobe ~ 40 kpc southeast of the core, as well as a bent radio jet connected to the radio core of NGC 5044 (Giacintucci et al. 2011). Although no X-ray cavity was directly detected at the position of this lobe, it was found to be correlated with a region of low IGrM abundances (David et al. 2011; O’Sullivan et al. 2014), while the bends in the radio jet and the inner edge of the lobe correlated with a sloshing front, suggesting that the radio structure had been shaped by IGrM motions (O’Sullivan et al. 2014). Of all the radio continuum observations to date, only the VLBA data show a consistent morphology at multiple frequencies, and only the GMRT 235 MHz data show a physically consistent correlation with the X-ray data.

To try to address these inconsistencies, we have acquired deep multiband radio observations of NGC 5044 using MeerKAT at L-band (0.85-1.67 GHz) and the upgraded GMRT in Bands 4 (550-850 MHz) and 3 (300-500 MHz). As well as offering significant increases in radio continuum sensitivity, the MeerKAT data provide an opportunity to search for neutral atomic gas in the galaxy via the HI line. Given the molecular and ionized gas observed in the cool cores of groups and clusters, neutral hydrogen must be present and may be a significant mass component of the gas produced through IGrM cooling. HI has been detected in absorption in ~ 20 brightest cluster galaxies (BCGs; see, e.g., Hogan 2014; Morganti & Oosterloo 2018; Saraf et al. 2023; Rose et al. 2024, and references therein) but detections in the dominant galaxies of X-ray luminous groups are rare, with only a handful of systems seen in absorption or emission (e.g., Jaffe & McNamara 1994; Morganti et al. 2006, 2009; Rose et al. 2024).

Throughout this paper, we adopt a flat Λ CDM cosmology with $H_0 = 70 \text{ km s}^{-1} \text{ Mpc}^{-1}$, $\Omega_m = 0.3$, and $\Omega_\Lambda = 0.71$. We adopt a redshift-independent distance of 31.2 Mpc for

NGC 5044 (Tonry et al. 2001) which corresponds to a physical scale of $1'' = 150 \text{ pc}$.

All output radio images are in the J2000 coordinate system and are corrected for primary beam attenuation. We define the radio spectral index, α , so that $S_\nu \propto \nu^\alpha$, where S is the flux density at frequency ν . Velocities quoted in this work are referenced with respect to the systemic heliocentric velocity of NGC 5044 using the optical definition. Following Schellenberger et al. (2020), we adopt a heliocentric systemic velocity of $cz = 2757 \text{ km s}^{-1}$. All HI uncertainties are given at the 1σ level throughout the paper.

2. OBSERVATIONS AND DATA REDUCTION

2.1. MeerKAT

We observed the NGC 5044 with MeerKAT in the L-band (Project code: SCI-20210212). An overview of the observation is given in Table 1. All four polarization products were recorded using the 32K correlator mode, covering a total bandwidth of 856 MHz with 32768 channels that are each 26.1 kHz wide. This corresponds to a velocity resolution of 5.5 km s^{-1} at $z = 0$. J0408-6545 and J1939-6342 were the primary calibrators used for flux density and bandpass calibration, observed at the beginning and end of the observing run. J1311-2216 was observed as a gain calibrator.

2.1.1. Continuum data reduction

The MeerKAT data covering a frequency range of 0.9-1.67 GHz were calibrated using the Containerized Automated Radio Astronomy Calibration (CARACal; Józsa et al. 2020) pipeline¹. The first step consists of flagging in CARACal, including shadowed antennas, autocorrelations, and known radio frequency interference (RFI) channels using the tfcrop algorithm. Thereafter, AOflogger (Ofringa et al. 2010) was used to flag bad data using the firstpass_QUV.rfis strategy. CARACal modeled the primary calibrator J0408-6545 using the MeerKAT local sky models. Following this, cross-calibration was performed to solve for the time-dependent delays and complex gains of each antenna and the bandpass corrections.

After initial calibration, we created an initial image of the target field using WSClean (Ofringa et al. 2014) within CARACal. Three rounds of phase-only self-calibration were performed using CubiCal (Kenyon et al. 2018), followed by a final round of amplitude-phase calibration. The calibrated data were imaged using the Briggs weighting scheme (Briggs 1995) with a robust parameter of 0, and multiscale cleaning. The properties of the MeerKAT continuum images are summarized in Table 2.

2.1.2. Line data reduction

¹ <https://ascl.net/2006.014>

Table 1. Observational overview: MeerKAT and uGMRT observations.

	MeerKAT	uGMRT	
	L-band	Band 4	Band 3
Observing date	June 8, 2021	December 2, 2023	January 23, 2018
	-	December4, 2023	January 24, 2018
Frequency coverage	0.85-1.67 GHz	550-950 MHz	300-500 MHz
Channel width	26.1 kHz	97 kHz	130.2 kHz
Number of channels	32768	4096	2048
On source time	4 hrs	10 hrs	4 hrs

Table 2. Continuum image properties

	Name	Restoring Beam	Robust parameter	uv -cut	uv -taper	RMS noise μ Jy beam ⁻¹
uGMRT Band3 (120-168 MHz)	IM1	10'' \times 10''	0	-	-	21
	IM2	15'' \times 15''	0	-	8''	23
	IM3	15'' \times 15''	0	≥ 0.2 k λ	8''	25
uGMRT Band 4 (550-750 MHz)	IM4	15'' \times 15''	0	-	8''	19
	IM5	15'' \times 15''	0	≥ 0.2 k λ	8''	21
MeerKAT L-band (0.9-1.6 GHz)	IM6	8.3'' \times 7.6''	-0.5	-	-	7
	IM7	15'' \times 15''	0	-	8''	8
	IM8	15'' \times 15''	0	≥ 0.2 k λ	8''	10

Notes. Imaging was always performed in WSCLEAN using multiscale and with Briggs weighting scheme.

We only proceed with the data covering the frequency range of 1200-1520 MHz to limit the computing resources required for calibration and imaging. The data were calibrated on the `ilifu` computer cluster hosted by the Inter-University Institute for Data Intensive Astronomy (IDIA).

Following Healy et al. (2021); Deb et al. (2022), we first performed the cross-calibration in CARACal (see Section 2.1.1 for details). The frequency range covering Galactic emission was flagged. The calibrated measurement set was binned in frequency by a factor of 5 (only for continuum calibration) to achieve a higher signal-to-noise ratio. The continuum imaging was performed in WSClean using Briggs weighting with a robust parameter of -0.5 , and uv taper of 10''. These parameters were chosen to achieve an optimal balance between angular resolution and sensitivity, with the uv taper specifically applied to recover low surface brightness continuum emission. The SoFiA (Serra et al. 2015) source finder, integrated into CARACal, was utilized to automatically produce a sky mask from the output deconvolved image. The self-calibration solutions were interpolated in frequency and transferred to the cross-calibrated target measurement set.

We subtracted the sky model using the task `mstransform` within CARACal and fitted a second-order polynomial fit to remove any residual continuum emission

from the spectral line data. The data were Doppler corrected to a barycentric reference frame. Finally, spectral line cubes (1370-1425 MHz) were created using WSClean Briggs weighting with a robust value of -0.5 and without any uv taper, giving an angular resolution of 8.3'' \times 7.6''. A number of galaxies in the group have been detected in the new MeerKAT observations. The H I results for other galaxies in the NGC 5044 group will be presented in a later paper. The final H I cubes were smoothed using binning and boxcart methods, as summarized in Table 3.

2.2. uGMRT

We observed the group NGC 5044 with uGMRT in Band 3 (Project code: 33_089) and Band 4 (Project code: 45_021) using the GMRT Wideband Backend (GWB) and GMRT software Backend (GSB). In both bands, observations were carried out in two observing runs, with 3C147 used as the flux density calibrator. The observational details are summarized in Table 1.

The uGMRT data calibration was performed using the Source Peeling and Atmospheric Modeling pipeline (SPAM Intema et al. 2009). The main steps are outlined below. Each wideband dataset was split into six sub-bands. The Band 4 data covering the frequency range 850-950 MHz were heavily affected by radio frequency interference and were thus

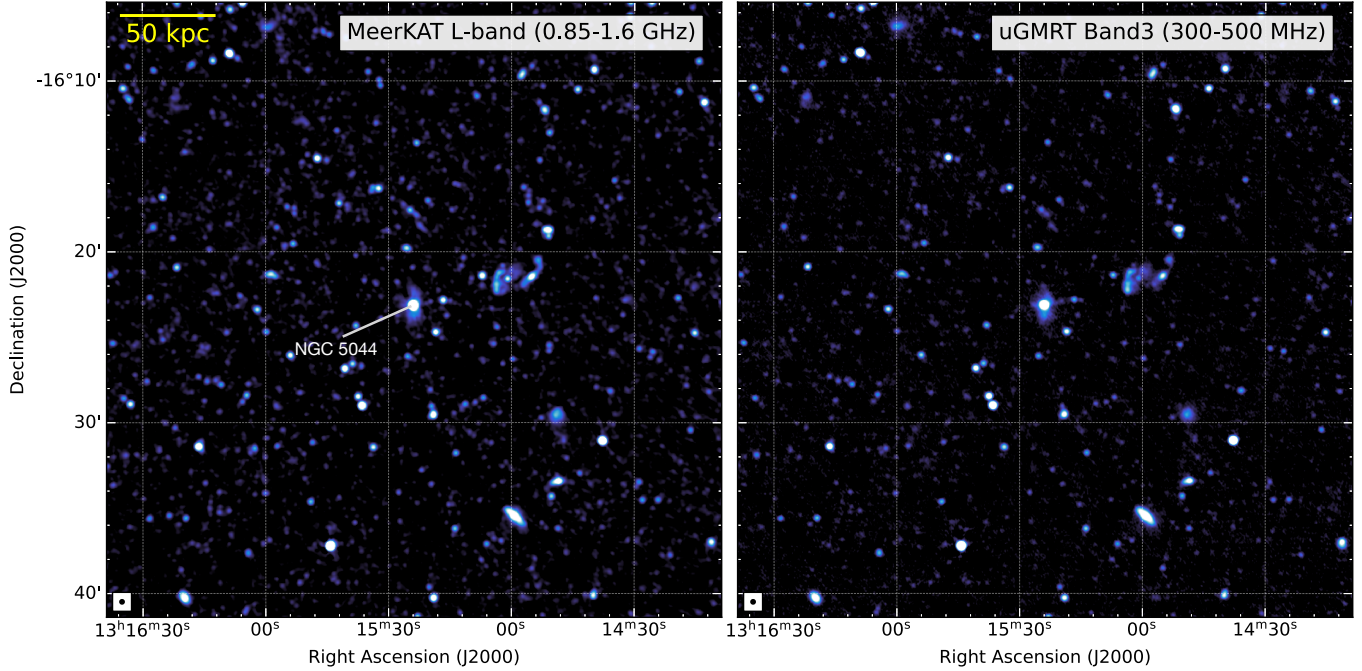


Figure 2. MeerKAT L-band (left) and uGMRT Band 3 (right) full band continuum radio images of the NGC 5044 field at a common resolution of $15''$. The radio beam size is indicated in the bottom left corner of each image. The image properties are given in Table 2, listed for IM2 and IM7.

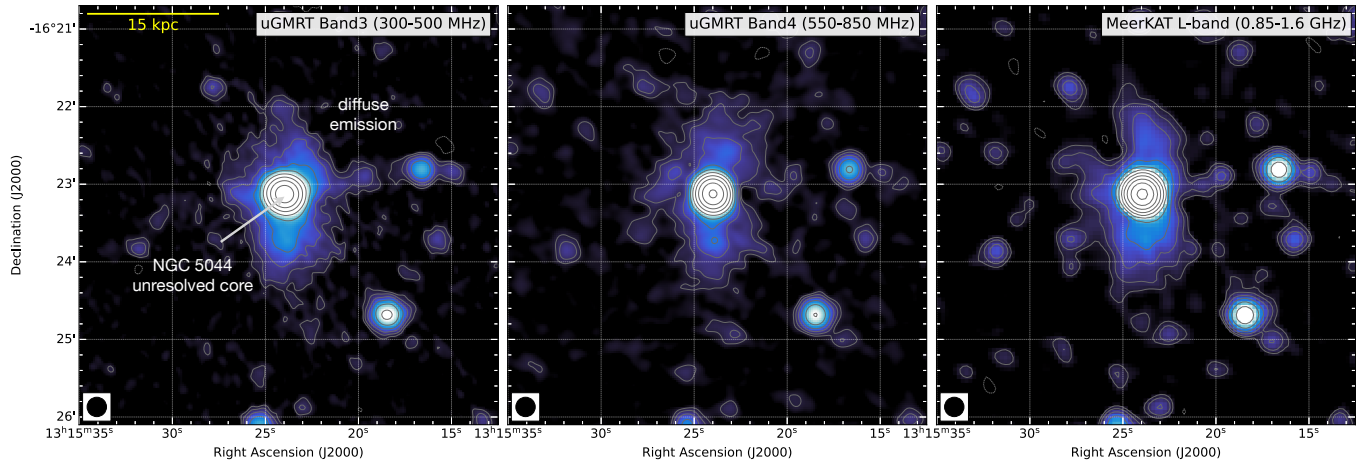


Figure 3. Zoomed-in uGMRT Band 3 (left), Band 4 (middle), and MeerKAT L-band (right) continuum images of NGC 5044, displayed on a square root scale. All images share a common resolution of $15''$. The beam size is indicated in the bottom left corner of each image. The images reveal diffuse radio emission surrounding NGC 5044 and extending almost 10 kpc from the galaxy in multiple directions. Radio contours are drawn at $[1, 2, 4, 8, \dots] \times 3.0\sigma_{\text{rms}}$. Dashed contours depict the $-3.0\sigma_{\text{rms}}$ contours. The image properties are given in Table 2, listed for IM2, IM4, and IM7.

flagged completely. The flux density of the primary calibrator 3C147 was set according to Scaife & Heald (2012). After flux density scale calibration, the data were averaged, flagged, and corrected for the bandpass. To correct the phase gains of the target field, we started with a global sky model obtained from the GSB data. In the end, the SPAM calibrated sub-bands were imaged in WSClean using Briggs weighting with robust parameter 0 to produce deep full continuum images. The final deconvolution was always performed using

multiscale, see Table 2 for uGMRT continuum image properties.

3. RESULTS AND ANALYSIS

3.1. Continuum Emission Properties

In Figure 2, we present our deep uGMRT Band 3 (300-500 MHz) and MeerKAT L-band (0.85-1.67 GHz) images covering a large field of view. A zoom-in of the central region is shown in Figure 3. These images have a common res-

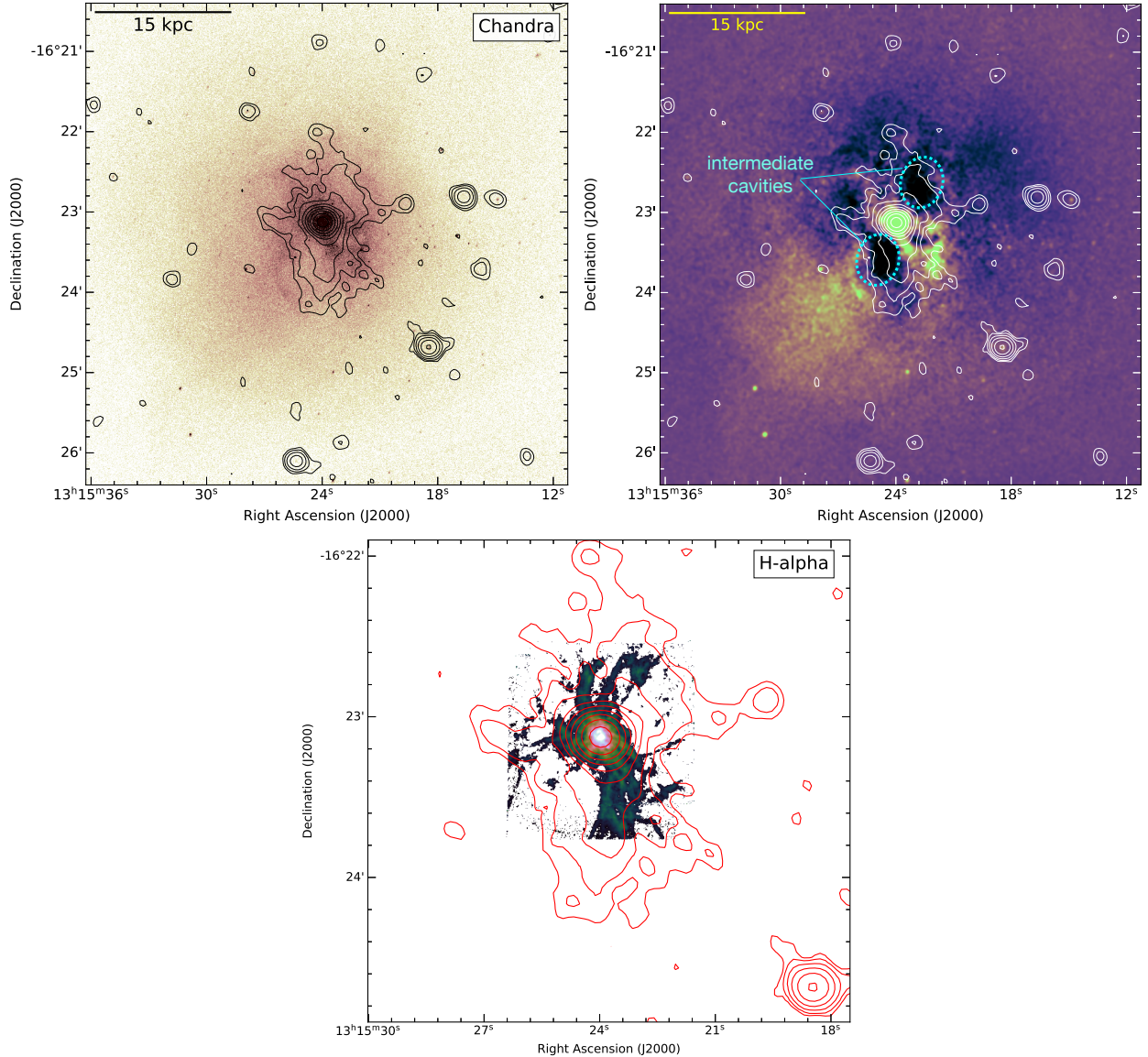


Figure 4. *Top Left:* Chandra 0.5 – 2 keV image of the galaxy group NGC 5044 overlaid with the uGMRT Band 3 10'' resolution contours. *Top Right:* Chandra 0.5 – 2 keV residual map, smoothed with a 2 pixel ($\sim 1''$) Gaussian and overlaid with the same uGMRT contours. The newly detected diffuse radio emission clearly fills the pair of intermediate cavities and extends beyond. *Bottom:* A zoom-in H α map of the NGC 5044 overlaid with the uGMRT contours. In contrast to the X-ray, the continuum and H α are spatially correlated, both are elongated in the north-south direction. In all maps, uGMRT Band 3 contour levels are drawn at $[1, 2, 4, 8, \dots] \times 3.0\sigma_{\text{rms}}$. The radio image properties are given in Table 2, IM1.

olution of $15''$. This resolution allowed us to recover the low surface brightness diffuse emission. Our new observations reveal, for the first time, diffuse radio emission surrounding the central AGN, with a largest linear size of approximately 25 kpc. The continuum emission is elongated along the north-south direction (Figure 3 right panel), in particular toward high frequencies. Unlike previously published continuum images, the detected radio emission displays a consistent morphology across all observed frequencies, as illustrated in Figure 3.

We do not detect any of the previously reported extended structures observed with the GMRT at 235 MHz and 610 MHz or with the VLA at 1.5 GHz (Giacintucci et al. 2009; Grossová et al. 2022). To investigate further, we reprocessed archival 235 MHz, 610 MHz, and 150 MHz GMRT observations using the SPAM pipeline that includes direction-dependent and ionospheric corrections (see Figure A.1 and Appendix for data used). The results are consistent with our new uGMRT and MeerKAT maps. We emphasize that our new uGMRT Band 3 images are a factor of five deeper than the previously published images at 235 MHz. The non-

Table 3. MeerKAT HI cubes properties

Frequency range	1370 – 1425 MHz
Velocity range	–966.5 to 11030.1 km s ^{–1}
Beam size	8.3'' × 7.6'', $d\nu = 5.5$ km s ^{–1} (rms = 0.2 mJy beam ^{–1})
Beam size	8.3'' × 7.6'', $d\nu = 27.9$ km s ^{–1} (rms = 0.1 mJy beam ^{–1} , binned)
Beam size	8.3'' × 7.6'', $d\nu = 16.7$ km s ^{–1} (rms = 0.2 mJy beam ^{–1} , boxcar smoothing)

Notes. All HI cubes are created with Briggs weighting with `robust` = –0.5 and without any uv-cut. All reported rms values represent per-channel noise levels. $d\nu$ is the velocity resolution.

detection of these features in both our new and archival data images suggests that those features are not real. We also re-processed archival VLA AnB configuration observations. In contrast to [Grossová et al. \(2022\)](#), we do not observe diffuse, jet-like emission extending east-west from the NGC 5044 core (see Figure A.2). Moreover, also in our high-resolution MeerKAT L-band image, we find no indication of the east-west jet-like emission (see Figure A.2).

In Figure 4 (top-left panel), we compare the radio and X-ray morphologies. A *Chandra* 0.5 – 2 keV map is overlaid with the uGMRT 380 MHz 10'' resolution contours. We used a higher resolution (10'') radio image, as it resolves certain radio structures and allows for a better comparison with X-ray features. Overall, the morphology of the newly detected radio emission does not correlate with the X-ray emission. Several structures are seen in the X-ray image with no clear radio counterpart. Moreover, on large scales (i.e., intermediate cavities and regions beyond them) there is only a partial correlation between radio and X-ray structures. In the top-right panel of Figure 4, we show a *Chandra* 0.5–2 keV residual map (obtained by subtracting the best-fitting elliptical β -model, convolved with the exposure map, from the merged image, [David et al. 2017](#)). Clearly, the newly detected radio emission extends significantly beyond the intermediate cavities (dashed cyan regions). The radio emission is moderately brighter in the northern intermediate cavity while it appears fainter (i.e., about a factor of 2 less brighter) and less prominent in the southern cavity. Although the cavities are fully filled by the radio emission, they (cavities) do not exhibit a clear connection to the overall radio morphology. In contrast to the radio and X-ray emission, there seems to be a spatial coincidence between the H α and the radio emission, as both are elongated in the north-south direction (see bottom panel of Figure 4).

To investigate the overall radio properties of the newly detected radio emission, we performed integrated and spatial

Table 4. Flux densities of the diffuse emission excluding the NGC 5044 core (i.e., within a 6.5 kpc diameter)

Frequency [MHz]	Flux density [mJy]
380	10 ± 1.0
675	6.9 ± 0.6
986	5.1 ± 0.5
1228	3.5 ± 0.1
1567	2.5 ± 0.1

Notes. Flux densities were measured from 15'' resolution images, created with Briggs weighting with `robust` = 0 and an common uv-cut of 200 $k\lambda$ (see Table 2, IM3, IM5, and IM8.). We assumed an absolute flux scale uncertainty of 10% for the uGMRT and MeerKAT UHF-band, and 5% for L-band.

spectral analyses. For the integrated radio analysis, we used wideband 15'' images at 380 MHz, 675 MHz, and 1.28 GHz, created with a uv-cut of 200 $k\lambda$ and Briggs weighting with `robust` = 0. The same images were used to produce a resolved spectral index map. To constrain the spectrum better, especially to check for a possible spectral break toward higher frequencies, we also include MeerKAT 986 MHz and 1.56 GHz sub-band images. The measured flux densities of the diffuse radio emission (i.e., excluding the contribution from the NGC 5044 core) are summarized in Table 4. The resulting integrated spectrum is shown in Figure 5 left panel, revealing a high frequency spectral steepening. At low frequencies, the spectral index is $\alpha_{380\text{ MHz}}^{986\text{ MHz}} = -0.70 \pm 0.05$, which steepens to $\alpha_{986\text{ MHz}}^{1.56\text{ GHz}} = -1.53 \pm 0.06$ at higher frequencies. The trends appear consistent with aging of electrons from AGN lobes owing to synchrotron and inverse Compton losses.

In Figure 5 right panel, we present the spectral index map of the central region of NGC 5044, created using maps between 380 MHz and 1.28 GHz. Pixels with flux density below $3\sigma_{\text{rms}}$ were blanked. We do not observe any specific trends across the diffuse emission, i.e., no clear evidence of spectral index gradients in a particular direction. The spectral age of the detected diffuse emission is determined by fitting the integrated spectrum of two subregions (only included diffuse emission) with a single injection Jaffe-Perola model (JP; [Jaffe & Perola 1973](#)). We emphasize that the compact core region of the NGC 5044 is excluded from the age analysis. Following [Brunetti et al. \(1997\)](#), for a power law energy distribution $N(E) \propto E^{-p}$, we estimated the magnetic field using the minimum-energy assumption:

$$B_{\text{eq,rev}} = D(p) \gamma_{\text{min}}^{\frac{2(2-p)}{p+5}} B_{\text{eq}, \frac{7}{p+5}}, \quad (1)$$

where B_{eq} is as follows:

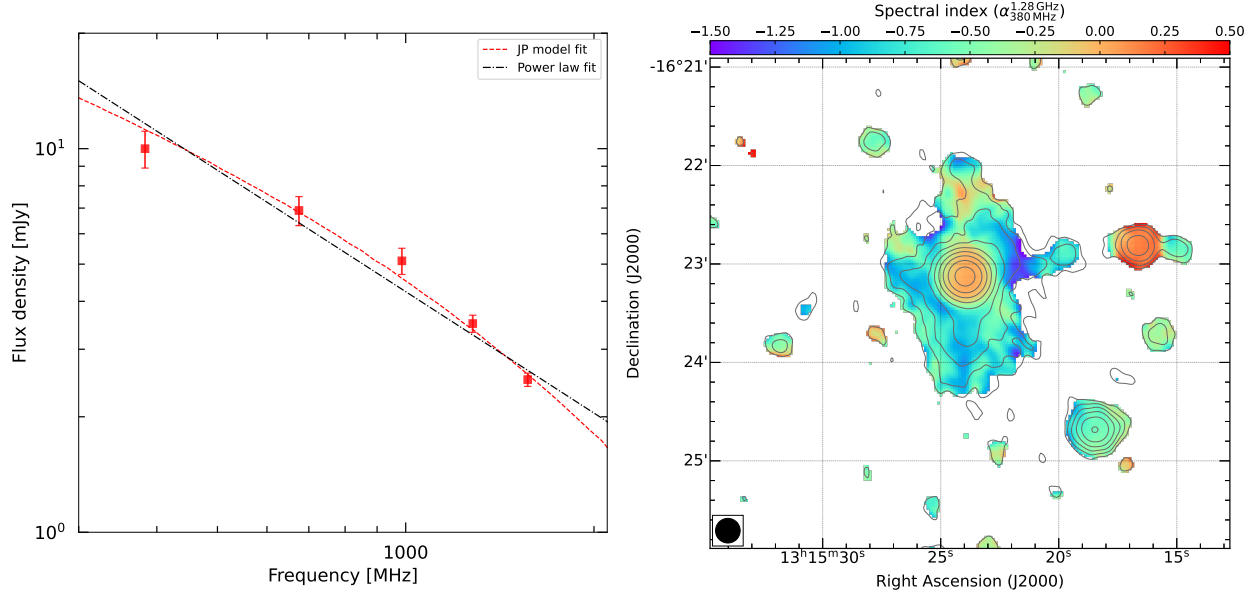


Figure 5. *Left:* Integrated spectrum of the newly detected diffuse radio emission excluding NGC 5044 core (i.e., within a 6.5 kpc diameter) between 380 MHz and 1.56 GHz. The dashed and dot-dashed lines represent the fitted JP model and a single power law, respectively. The JP model fitting is performed in `synchrofit`. *Right:* Spectral index map at $15''$ resolution created between 380 MHz and 1.28 GHz, showing no particular trends. Radio contour levels are drawn at $[1, 2, 4, 8, \dots] \times 3.0\sigma_{\text{rms}}$. The image properties are given in Table 2, listed for IM3 and IM8.

$$B_{\text{eq}} = 5.69 \times 10^{-5} \left[\frac{(1+k)}{\eta} (1+z)^{3-\alpha} \frac{1}{\theta_x \theta_y l \sin^{3/2} \phi} \times \frac{S_{\text{obs}} \nu_2^{0.5+\alpha} - \nu_1^{0.5+\alpha}}{\nu_{\text{obs}}^{+\alpha} 0.5+\alpha} \right]^{2/7} \text{ Gauss.} \quad (2)$$

θ_x and θ_y represent the angular dimensions of the radio source in arcseconds along the x- and y-axes, respectively. k is the proton-to-electron energy ratio, η is the filling factor of the emitting region, and l denotes the path length through the source in kiloparsecs. S_{obs} is the radio flux density (in Jy) of the region at the observed frequency ν_{obs} (in GHz). ν_1 and ν_2 are the pre-assumed lower and upper cut-off frequencies for the radio spectrum (in GHz). ϕ is the angle between the magnetic field and the line of sight. The particle energy distribution index, p , is given by $p = 1 - 2\alpha$, and γ_{min} represents the minimum Lorentz factor of the particle distribution.

We use a spectral index of -0.55 (i.e., injection index obtained by fitting the spectrum with the JP model using `synchrofit`²), $\nu_1 = 0.010$ GHz, $\nu_2 = 100$ GHz, $S_{\text{obs}} = 9.9$ mJy, $\nu_{\text{obs}} = 0.380$ GHz, and assume $k = 1$, $\eta = 1$. For size, we adopted $\theta_x = 66''$ and $\theta_y = 110''$, and the radial direction $l = 9.9$ kpc (assuming l is equal to the transverse direction), all measured from the uGMRT Band 3 map, and excluded the NGC 5044 core region. Following Brunetti et al. (1997), we adopt $D(\gamma) = 1.01$ and $\gamma_{\text{min}} = 20$. This

gives us the revised equipartition magnetic field value of $B_{\text{eq,rev}} = 1.4 \mu\text{G}$, resulting in an estimated mean spectral age of 77 ± 10 Myr. Additionally, we also consider a magnetic field value that minimizes the radiative losses and maximizes the lifetime of the source ($B = B_{\text{CMB}}/\sqrt{3}$ where $B_{\text{CMB}} = 3.25(1+z)^2$ is the equivalent magnetic field of the cosmic microwave background), estimated to be approximately $1.9 \mu\text{G}$. This yields a mean spectral age of about 80 ± 15 Myr.

3.2. HI Properties

In Figure 6, we show our HI moment zero map (i.e., integrated intensity) from the MeerKAT HI cube centered on the core which reveals HI absorption detected towards NGC 5044. The HI cube was binned to a velocity resolution of 27.9 km s^{-1} (i.e., 5 channel binning) to enhance the sensitivity of the data. The HI absorption is concentrated within the core region, i.e., within the central 800 pc ($5.4''$) diameter.

Figure 7 (left panel) shows the resulting HI spectrum, generated in `SoFIA` by integrating over a 2D mask (a circle with a radius of $4.2''$, which is similar to the beam size) centered on NGC 5044 in each channel. The spectrum shows a pronounced absorption feature at 286 km s^{-1} . The detection has a significance of 3.8σ (99.9% confidence).

We also applied Boxcar smoothing to assess the robustness of the detected HI absorption feature. Using a 3-channel kernel, this smoothing resulted in a velocity resolution of 16.7 km s^{-1} . This resolution was specifically chosen to investigate the potential presence of double absorption fea-

² <https://github.com/synchrofit/synchrofit>

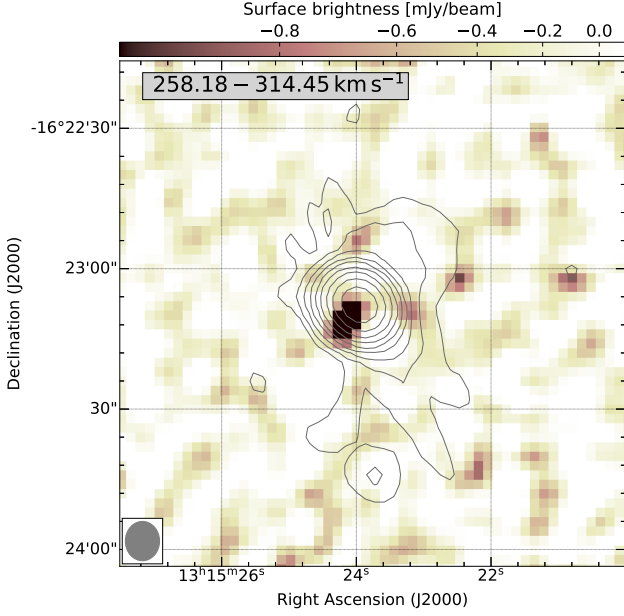


Figure 6. H I moment zero MeerKAT map ($8.3'' \times 7.6''$) showing absorption from the core of NGC 5044 overlaid with continuum emission contours at 1.28 GHz ($8.3'' \times 7.6''$). The H I cube was binned to a velocity resolution of 27.9 km s^{-1} (5 channel binning). The image reveals the H I absorption from the core region of NGC 5044. Contour drawn at $[1, 2, 4, 8, \dots] \times 5.0\sigma_{\text{rms}}$ where $\text{rms} = 12 \mu\text{Jy beam}^{-1}$.

Table 5. Gaussian fits to the H I and CO absorption features

	Velocity (km s^{-1})	FWHM (km s^{-1})	Amplitude (mJy)
H I	280.1 ± 2.1	14.2 ± 5.4	0.68 ± 0.19
	297.5 ± 1.7	7.6 ± 2.3	0.85 ± 0.2
CO	286.1 ± 0.3	6.7 ± 0.7	9.5 ± 0.7
	295.5 ± 0.4	6.4 ± 0.9	7.2 ± 0.7

Notes. Double Gaussian fit for the H I spectrum is extracted within an aperture representing the beam size. The cube has a beam size of $8.3'' \times 7.6''$, velocity resolution 5.5 km s^{-1} , and rms $0.2 \text{ mJy beam}^{-1}$. We emphasize that the CO spectrum is adopted from Schellenberger et al. (2021) but using the optical velocity definition.

tures, as seen in the CO observations. The corresponding spectrum is shown in Figure 6 right panel and reveals a double absorption dip structure. We note at the same velocity resolution, the binning method also reveal the double-dip absorption features, further affirming the presence of double-peaked absorption.

3.2.1. H I column density

The column density of the H I absorption feature is estimated as:

$$\frac{N_{\text{HI, abs}}}{\text{cm}^{-2}} = 1.82 \times 10^{18} \left(\frac{T_{\text{spin}}}{\text{K}} \right) \int \tau \left(\frac{dv}{\text{km s}^{-1}} \right), \quad (3)$$

where T_{spin} is the spin temperature representing the weighted harmonic mean of the various thermal components of H I. The $\int \tau dv$ is the optical depth of the H I absorption calculated as:

$$\int \tau dv = \sum_{i=1}^n -\ln \left(1 - \frac{f_i}{S} \right) \times \Delta v, \quad (4)$$

where f_i is the H I absorption flux density in Jy at frequency channel i , n is the number of channels where absorption is seen, S is the continuum flux density in Jy, and Δv is the width of each channel in km s^{-1} . We measure a continuum flux density of $31 \pm 2 \text{ mJy}$ (extracted from the full wideband image) at 1.4 GHz. Substituting $\Delta v = 5.5 \text{ km s}^{-1}$ and other values in Equation 4, we calculate $\int \tau dv = 0.526 \pm 0.103 \text{ km s}^{-1}$. This optical depth corresponds to an H I absorption column density of $N_{\text{HI, abs}} = 9.58 \pm 1.87 \times 10^{17} T_{\text{spin}} \text{ cm}^{-2}$. To accurately constrain the H I column density, it is crucial to estimate the spin temperature. For instance, a dense cold neutral medium is characterized by spin temperatures in the range $100 \leq T_{\text{spin}} \leq 1000 \text{ K}$ (Wolfire et al. 1995), whereas the warm neutral medium exhibits significantly higher spin temperatures, ranging from $5000 \leq T_{\text{spin}} \leq 8000 \text{ K}$.

The spin temperature can be directly estimated from the ratio of the emission and absorption column densities, where the H I emission column density is given by (Allison 2021):

$$N_{\text{HI, em}} = 1.823 \times 10^{18} \int T_B dv, \quad (5)$$

where T_B is the brightness temperature in units of K. The above equation is derived under the assumption that the background radiation is negligible and approximating $T_{\text{spin}} \int \tau_{\text{HI}} dv \approx \int T_B dv$ (for details see Meyer et al. 2017; Allison 2021). The velocity integrated T_B can be calculated as :

$$\int T_B dv = 1.36 \times \lambda^2 \times \frac{1}{\theta_a \theta_b} S_{\text{int}}, \quad (6)$$

where $S_{\text{int}} = \int S_\nu dv$ is the integrated H I emission flux density in mJy km s^{-1} , θ_a and θ_b are the full width at half-maximum (FWHM) of the synthesized beam in arcsec. However, as the 21 cm line was not detected in emission, we can only put an upper limit on the spin temperature. The 3σ upper limit for the integrated line flux density is $S_{\text{int}} \leq 0.0522 \text{ Jy km s}^{-1}$ (see the next section). Putting this S_{int} value, $\theta_a = 8.3''$, $\theta_b = 7.6''$, and $\lambda = 21.1 \text{ cm}$ (for H I line) in Equation 6, we obtain the upper limits $T_B \leq 500 \text{ K}$ and

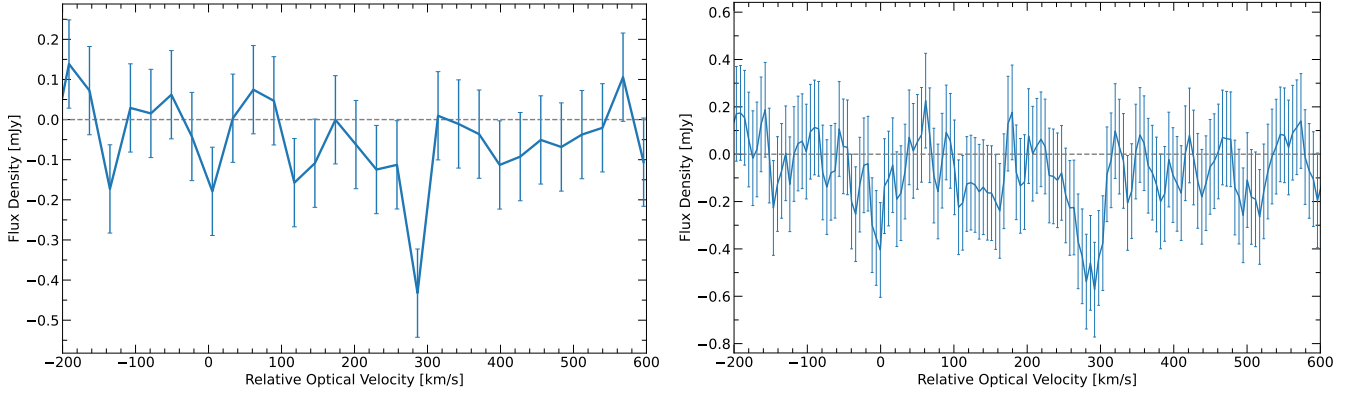


Figure 7. H I absorption spectra toward the compact core of NGC 5044 obtained from SOFIA. Both spectra are extracted from an H I cube with beam size of $8.3'' \times 7.6''$ using a circular region of radius $4.2''$, i.e. similar to the beam size. *Left:* Spectrum obtained by applying 5-channel binning, resulting in an effective velocity resolution of 27.9 km s^{-1} . The rms noise of the H I cube is $0.1 \text{ mJy beam}^{-1}$. *Right:* The spectrum was obtained by performing Boxcar smoothing with a 3-channel kernel, resulting in an effective velocity resolution of 16.7 km s^{-1} .

$N_{\text{H I,em}} \leq 9.13 \times 10^{20} \text{ cm}^{-2}$. By dividing this column density by our estimated absorption column density, we get the spin temperature upper limit of $T_{\text{spin}} \leq 950 \text{ K}$, suggesting that the detected H I is in the cold neutral phase. Schellenberger et al. (2020) obtained a molecular hydrogen column density of $N_{\text{H}_2} \approx 1.5 \times 10^{20} \text{ cm}^{-2}$, from the CO absorption.

3.2.2. H I mass upper limit

In our MeerKAT L-band observation, no H I emission is detected toward NGC 5044. We place an upper limit on the H I gas mass from the non-detection:

$$\frac{M_{\text{H I}}}{M_{\odot}} = \frac{2.36 \times 10^5 D_{\text{L}}^2}{(1+z)} \int S_{\nu} dv, \quad (7)$$

where $\int S_{\nu} dv$ is the integrated line flux density in Jy km s^{-1} and D_{L} is the luminosity distance to the galaxy in Mpc. We derived a 3σ upper limit for the integrated flux density $\int S_{\nu} dv = 3\sigma_{\text{rms}} \sqrt{N} \Delta v$, where N is the number of channels that the galaxy would span, σ is the noise per channel and Δv is the channel width. Following Schellenberger et al. (2020), we determined N using the CO(2-1) emission velocity range which spans from -520 and 330 km s^{-1} . This results in $\int S_{\nu} dv < 0.0522 \text{ Jy km s}^{-1}$ (within $4.2''$ radius aperture). Since the CO integrated flux density was estimated within a $15''$ radius aperture, we also apply the same aperture, yielding $\int S_{\nu} dv < 0.2367 \text{ Jy km s}^{-1}$. Substituting $D_{\text{L}} = 31.2 \text{ Mpc}$ and other relevant parameters into Equation 7, we obtained an H I mass upper limit of $M_{\text{H I}} < 1 \times 10^7 M_{\odot}$ ($4.2''$ radius aperture) and $M_{\text{H I}} < 5.4 \times 10^7 M_{\odot}$ ($15''$ radius aperture).

Schellenberger et al. (2020) reported a molecular mass of $M_{\text{H}_2} = 9.5 \pm 1.2 \times 10^7 M_{\odot}$ in a $15''$ radius aperture using the standard Milky Way CO-to-H₂ conversion factor of $X_{\text{CO}} = 2 \times 10^{20} \text{ cm}^{-2} (\text{K km s}^{-1})$. This implies that the ratio of molecular to atomic gas in the central 2.2 kpc of NGC 5044 is $>1.76:1$. We note that it is unclear whether the

Galactic conversion factor is applicable in the cooling cores of galaxy clusters and groups. As yet only one measurement is available, which finds a value a factor of 2 lower (Van-tyghem et al. 2017), but more measurements are needed to determine whether this is representative of the population as a whole. In NGC 5044, we can only note that the molecular gas mass could be a factor of 2 lower, in which case our H I mass upper limit could be comparable to the measured H₂ mass.

3.2.3. H I and CO(2-1) comparison

In Figure 8, we compare the H I spectrum with the CO(2-1). Clearly, the H I absorption feature has a counterpart in CO(2-1) and is moderately broader. We fit the H I absorption features with a double Gaussian model. For fitting we extracted the spectrum from the unsmoothed cube (i.e., 5.5 km s^{-1} velocity resolution) which is essential for accurately determining the intrinsic shapes and widths of the spectral features. The resulting fit is shown in the bottom panel of Figure 8. The fitting yields velocities of $280.1 \pm 2.1 \text{ km s}^{-1}$ and $297.5 \pm 1.7 \text{ km s}^{-1}$, comparable to the CO(2-1) velocity values. In Table 5 we present the FWHM and velocities of each Gaussian component.

Comparing the 27.9 km s^{-1} smoothed H I spectrum (Figure 7 left panel) reveals that its peak velocity aligns closely with one of the two CO(2-1) absorption peaks at 286.1 km s^{-1} . The higher-resolution 5.5 km s^{-1} H I spectrum (Figure 8) reveals a double-dip and one of them approximately corresponds to the velocity of the CO absorption features (indicated by green dashed lines; see also Table 5).

4. DISCUSSION

4.1. Origin of the diffuse radio emission

As noted in Section 1, the radio structure of NGC 5044 has been a subject of some debate, with only the VLBA observations of the parsec-scale core and jets providing a con-

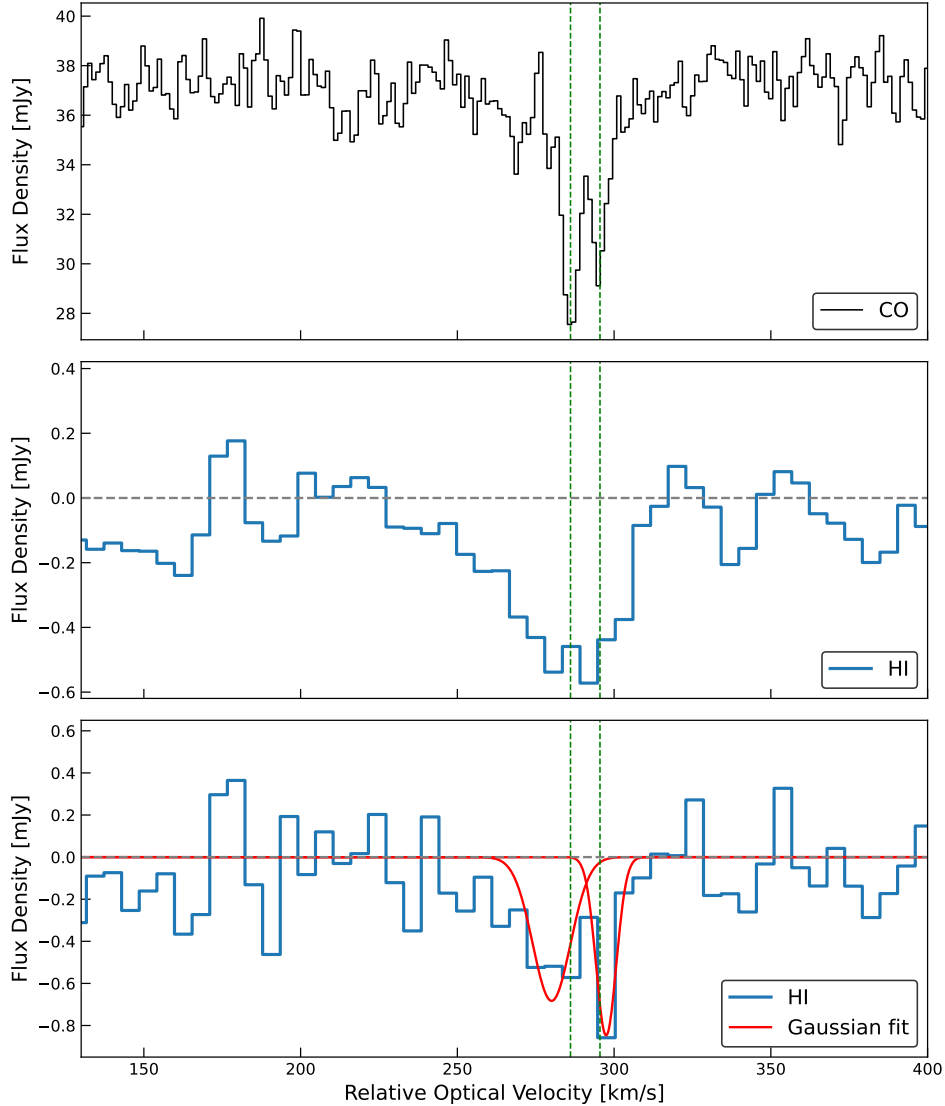


Figure 8. CO (top) and H I (middle/bottom) absorption spectra from the nuclear region of NGC 5044. The raw H I spectrum is shown in the lower panel, and the middle panel shows the spectrum, boxcar smoothed to a velocity resolution of 16.7 km s^{-1} . The CO spectrum, adopted from Schellenberger et al. (2020), shows two strong absorption features peaks at $\nu = 286.1 \text{ km s}^{-1}$ and 295.5 km s^{-1} (green dashed lines). The H I absorption also shows a double-dip and exhibits a broader tail toward lower velocities compared to the CO. The two-Gaussian H I components are shown in red (bottom) and the values are given in Table 5. H I spectra (middle and bottom) are extracted within $4.2''$ radius.

sistent picture at multiple frequencies. On scales larger than a kiloparsec, prior published observations at different frequencies presented different radio structures, with only partial correlations with the cavities and filaments observed in the hot, X-ray emitting IGrM (Giacintucci et al. 2011; David et al. 2011; O’Sullivan et al. 2014; Grossová et al. 2022). Several factors may have contributed to this lack of consistency between the published radio images, and between them and our new analysis: 1) the relative faintness of the diffuse emission in NGC 5044, only $\sim 1 \text{ mJy b}^{-1}$ at L-band for the brightest areas; 2) the relatively shallow older archival VLA and GMRT observations, made prior to broad-band upgrades which dramatically improved the uv-coverage and sensitiv-

ity of these telescopes; 3) the advent of, and improvements in, tools for ionospheric modeling and direction-dependent calibration; 4) Advancements in data reduction pipelines and particularly new image reconstruction algorithms (that use, for instance, the multiscale option, which is crucial to properly image low surface brightness extended radio structures) as well as efficient, automated RFI flagging, especially at low frequencies. The improvements in telescope sensitivity and data reduction methods played a significant role in motivating us to acquire the new data presented in this paper.

These new data provide a consistent view of the diffuse radio emission on scales of order 10 kpc, with good agreement across a wide frequency range, and reanalysis of the

archival data with modern tools shows that the older data are consistent with the new data. We can, therefore, be confident of the radio morphology presented here. However, our new images reveal that the diffuse radio emission is poorly correlated with the hot IGrM, overlapping the cavities but extending beyond them. The emission in and around the cavities has some of the steepest spectral indices, but the spectral index distribution is also poorly correlated with the X-ray morphology. The estimated radiative spectral age for the radio emission (77 ± 10 Myr) is significantly higher than the timescales previously determined for the formation of the ~ 5 kpc-scale cavities (~ 10 -20 Myr, David et al. 2009; O’Sullivan et al. 2011). However, the latter were estimated assuming cavity expansion at the sound speed and, given the lack of shock heated rims around the cavities, they must be underestimates. The buoyant and sonic timescales for these cavities are comparable, but the refill timescale is significantly longer (~ 30 -35 Myr) and gas motions may have affected the expansion and rise of the cavities, rendering such dynamical estimates inaccurate. It should also be noted that these dynamical estimates assume the cavities to be located in the plane of the sky, and are thus effectively lower limits; if the cavities are inclined toward the line of sight (i.e., in front of or behind the galaxy core) their dynamical ages would be greater. For the limiting plane-of-sky case, to bring the radio age estimate into agreement with the cavity refill timescale would require a magnetic field of $B \simeq 7 \mu G$ or $0.2 \mu G$, which is plausible for a dominant group galaxy. Agreement with the shorter buoyant and sonic timescales would require $B \simeq 12$ – $20 \mu G$.

While the inflation of cavities by expanding radio lobes means that we expect radio emission to be confined within the X-ray structure, NGC 5044 is not alone in showing morphological disagreements. Among galaxy groups, NGC 1407 and NGC 3411 (also known as NGC 3402 or SS2b 153) both host large (~ 80 kpc) diffuse, steep spectrum ($\alpha = -1.8$ and -1.4 , respectively) radio structures which surround the group-dominant galaxy and have no corresponding cavity or rim structures in the X-ray (O’Sullivan et al. 2007; Giacintucci et al. 2011, 2012). For NGC 1407, there is evidence that the emission arises from old lobe plasma, and NGC 3411 shows at least some bipolar symmetry that might indicate a similar origin. However, Giacintucci et al. (2011) compared their radio morphology to that of radio mini-halos seen in galaxy clusters. NGC 777 provides a smaller example, with symmetrical ~ 10 kpc-scale diffuse emission surrounding its radio core, located within an X-ray channel that probably indicates that the radio plasma is the remnant of old, faded lobes (O’Sullivan et al. 2024). By contrast, the group-dominant galaxies NGC 677 and NGC 1587 (Giacintucci et al. 2011; Kolokythas et al. 2018, 2019) host distinctly asymmetric diffuse emission structures on scales of 5-10 kpc, again with no clear correlation with the hot IGrM.

These structures are detected at a single frequency and they do not appear consistent with typical jets or lobes. Further observations are needed before their origin can be determined. IC 1860 provides an example of a slightly different phenomenon; it hosts a ~ 35 kpc diffuse radio trail extending southeast from its core, but while this is not correlated with any cavities, it is aligned with the innermost part of a sloshing spiral, and probably represents old lobe material drawn out by the IGrM motions (Gastaldello et al. 2013).

Examples of complex radio/X-ray morphologies in galaxy clusters include 2A 0335+096, which contains a complex collection of at least five cavities whose development may have been affected by sloshing motions in the ICM (Sanders et al. 2009). An inner double radio source is closely correlated with two of these, but diffuse low frequency radio emission overlaps the remaining three and extends well beyond (Bîrzan et al. 2020; Kokotanekov et al. 2017). Perhaps most famously, ultra-deep high resolution X-ray mapping of the core of the Perseus cluster has revealed multiple cavities whose positions and morphologies have likely been affected by sloshing motions in the ICM. Two pairs of cavities are clearly correlated with the inner and outer radio lobes of NGC 1275, but diffuse radio emission extends well beyond those structures, with filaments linking them to the older "ghost" cavities, and eventually merging with the surrounding mini halo (van Weeren et al. 2024; Kokotanekov et al. 2017).

These examples make clear that extended radio structures in group and cluster-central galaxies are often more complex than simple cavity-filling lobes. The origin of the more extended emission is not always clear. In cool core clusters, the AGN is not always the dominant source of extended radio emission. Centrally located steep spectrum diffuse radio sources, known as mini-halos, are observed to extend up to 500 kpc, and are often bounded by sloshing fronts in the ICM. The exact nature of the processes responsible for the relativistic electron population in these sources is still under debate (e.g., Giacintucci et al. 2019; Ignesti et al. 2020), but ICM turbulence associated with sloshing motions appears to play a role. However, in groups the gas turbulent motions are thought to be insufficient (Brunetti & Jones 2014). No mini-halos have yet been observed in groups, and the emission we observe in NGC 5044 is not consistent with a mini-halo; its size, radio power, and radio emissivity are not compatible with the known relationship for mini-halos (Murgia et al. 2009), and the radio and X-ray surface brightness are not correlated.

Perhaps a more likely possibility is that the radio emission reveals plasma, originally in radio jets or lobes, but which has now diffused out into the surrounding IGrM. The deep *Chandra* observations of NGC 5044 have revealed its core to be highly structured, with cavities, channels and filaments

of thermal plasma probably shaped by the IGrM “weather”, driven by the combination of AGN heating, buoyant forces, and sloshing (e.g., David et al. 2011, 2017). The overall correlation between the H α nebula and the diffuse radio structure (Figure 4 bottom) could also indicate that the same gas motions shape the two. There is extensive observational evidence of the impact of sloshing on the development of central radio sources. In addition to the examples given above, NGC 507 provides a prime example of a galaxy group where sloshing has affected both lobe shape and the morphology of plasma filaments which appear to trace material leaking from those lobes (Brienza et al. 2022). Disruption of radio structures by ICM/IGrM motions is also predicted by some simulations (e.g., Morsony et al. 2010; Bourne & Sijacki 2017), with weaker jet sources (such as that in NGC 5044) expected to be more strongly affected (Bourne & Sijacki 2021). However, the processes involved are not sufficiently well understood for us to know whether “weather” in the core of NGC 5044 could drive the degree of mixing necessary to produce the radio morphology, and the poor correlation with the X-ray morphology, which we observe.

4.2. Cold gas content: comparison with other systems

Although a significant fraction of early-type galaxies are found to contain cold gas reservoirs, the mass of cold gas is generally lower than that found in late-type galaxies of comparable mass, and gas content is strongly correlated with the environment, with satellite galaxies in dense environments typically hosting smaller quantities of more disturbed gas (Young et al. 2011; Serra et al. 2012; Davis et al. 2019). Environmental effects have been found on the group scale, with the cold gas content of individual galaxies and of the group as a whole declining with increasing mass (Kilborn et al. 2009; Desjardins et al. 2014; Odekon et al. 2016). There are relatively few systematic comparisons of atomic and molecular gas content, but Welch et al. (2010) found that M_{H_2}/M_{H_1} in early-type field galaxies tend to cluster around either 0.05 or 0.5, and Obreschkow & Rawlings (2009) report $M_{H_2}/M_{H_1} \sim 0.5$ for ellipticals. The lower limit we derive for NGC 5044, $M_{H_2}/M_{H_1} > 1.76$, is consistent with a handful of early-type galaxies at the high end of the range found by these previous studies.

There is morphological and kinematic evidence that many early-type galaxies acquired their cool gas through mergers with, or tidal stripping of, gas-rich neighbors (e.g., Serra et al. 2012; Maccagni et al. 2023). Some group-dominant galaxies also have the disturbed gas structures characteristic of such interactions (e.g., O’Sullivan et al. 2018; Olivares et al. 2022), but the filamentary nebula in NGC 5044 shows very clearly that its cold gas is the product of cooling from the IGrM. Rose et al. (2024) point out that in group and cluster-dominant galaxies, molecular absorption lines

seem to arise from two populations of molecular gas clouds. Clouds with low velocity dispersion, small velocity offsets from the galaxy, and a lack of any systemic velocity flow are likely located in stable rotating disks. Clouds with higher velocity dispersions tend to show higher velocity offsets, and in the Rose et al. (2024) sample are universally redshifted, indicating that they are infalling material located closer to the AGN.

Of the other group-dominant galaxies in which HI absorption has been detected, hydrogen column densities in the range $N_{H_1,abs} = 2.5 - 7 \times 10^{18} T_{spin} \text{ cm}^{-2}$ are found in NGC 4261 and NGC 315 (Jaffe & McNamara 1994; Morganti et al. 2009), comparable with if somewhat greater than the column density we observe in NGC 5044. NGC 4261 and NGC 6868 both show line profiles with components centered around the systemic velocity (Rose et al. 2024; Jaffe & McNamara 1994). Both also show rotating disks in molecular emission, suggesting that the HI is likely associated with the disk (e.g., Ruffa et al. 2019a,b). NGC 315 also hosts a molecular gas disk (Boizelle et al. 2021) but has a more complex HI absorption structure, with a narrow (FWHM=2.5 km s $^{-1}$) absorption line redshifted by ~ 490 km s $^{-1}$ relative to the systemic velocity (Dressel et al. 1983) and a somewhat broader (FWHM=80 km s $^{-1}$) absorption component redshifted by only ~ 80 km s $^{-1}$ (Morganti et al. 2009). HI is also seen in emission a few kiloparsecs from the NGC 315 nucleus, at velocities extending up to that of the narrow absorption line. Morganti et al. (2009) conclude that the broader absorption likely arises from gas close to the nucleus, and perhaps in the nuclear disk, while the narrow line probably traces an infalling gas cloud located further away, either originating from IGrM cooling, or acquired via tidal stripping.

NGC 5044 is different from these systems. The redshifted velocity and moderately broadened velocity dispersion of the CO absorption line has been interpreted as indicating that the molecular clouds responsible are not part of a disk, and are likely infalling toward the AGN (David et al. 2014; Schellenberger et al. 2020; Rose et al. 2024). Based on the velocity of the clouds and their evaporation timescale, Schellenberger et al. (2021) argued that they are very likely to be within the gravitational sphere of influence of the SMBH, which they estimated as having a radius ~ 22 pc, based on a black hole mass $M_{SMBH} = 2.3 \times 10^8 M_{\odot}$. Diniz et al. (2017) find a black hole mass an order of magnitude higher, $M_{SMBH} = 1.8 \times 10^9 M_{\odot}$, and Schellenberger et al. (2024) find comparable values based on modelling of the radio to sub-millimeter spectral energy distribution. This strengthens the original argument, making it near-certain that the CO and HI absorption features arise from gas clouds well inside the SMBH sphere of influence.

The molecular-to-atomic gas mass ratio we find for NGC 5044 would be unusually high if it had acquired its

gas from another galaxy, but is consistent with the prediction of the chaotic cold accretion (CCA) model advanced by Gaspari et al. (2017). From simulations of the thermally unstable IGrM in the central 2 kpc of a group-dominant galaxy (using a region and parameters chosen to allow comparison with NGC 5044), Gaspari et al. (2017) found a mass ratio $M_{H_2}/M_{H I}$ increasing from ~ 1 at early times to ~ 4 after 70–80 Myr of cooling. The mass of the warm ionized component was a factor ~ 10 lower than that of the neutral atomic gas. Interestingly, this suggests that it should be practical to detect the neutral phase in emission in NGC 5044. If HI is present in the quantities the CCA model predicts, we would only need to improve on the mass sensitivity of our MeerKAT observation by a factor ~ 2.3 to detect it.

5. CONCLUSIONS

We reported wideband multifrequency radio observations (continuum and H I) of NGC 5044, the dominant elliptical of the X-ray brightest group in the sky. These observations were conducted with the uGMRT (300–850 MHz) and MeerKAT (850 MHz to 1.67 GHz). Our new observations reveal diffuse radio emission extending to ~ 25 kpc from the radio core. This emission is only weakly correlated with the IGrM morphology and extends well beyond the known X-ray cavities. It shows a strongly curved radio spectrum, relatively flat at low frequencies ($\alpha_{380\text{ MHz}}^{986\text{ MHz}} = -0.70 \pm 0.05$) but steepening at high frequencies ($\alpha_{986\text{ MHz}}^{1.56\text{ GHz}} = -1.53 \pm 0.06$). Using a revised equipartition magnetic field of $B = 1.4 \mu\text{G}$, the estimated radiative spectral age is around 77 – 80 Myr. We suggest that this newly detected diffuse radio emission likely originated as relativistic plasma of the AGN jets or lobes, which has since diffused into the IGrM by gas motions or “weather” driven by the combination of AGN heating, tidal sloshing, and radiative cooling. NGC 5044 is not alone among groups or clusters in hosting complex diffuse radio emission which is not confined within clear cavities. As the sensitivity of radio observations improves, it is likely that such emission will be discovered in an increasing number of systems.

We also report the first detection (at 3.8σ level) of neutral atomic gas in the cooling region of NGC 5044, in the form of a double-structured H I line seen in absorption against the radio core of NGC 5044. The velocities of the H I peaks are consistent with those of the CO(2-1) absorption lines previously reported in the galaxy, suggesting that both sets of lines trace different density zones of the same gas clouds. The HI lines show moderately broader velocity dispersions compared to the CO(2-1), consistent with our expectations in this scenario. We find the column density and velocity width of the HI lines to be comparable to those seen in the handful of other cool-core systems where HI is detected in absorption, and conclude that the clouds are likely inside the sphere of

influence of the central SMBH and infalling onto the AGN, as suggested by previous studies. From the non-detection of the H I emission in the core of NGC 5044, we place an upper limit on the atomic mass of $M_{H I} < 5.4 \times 10^7 M_{\odot}$ in the central 2.2 kpc ($15''$). The molecular-to-atomic mass ratio ($M_{H_2}/M_{H I} \gtrsim 1.7$) aligns with predictions of the chaotic cold accretion model, which implies that only modest increases in sensitivity may be needed to detect the HI emission from the neutral atomic phase of the cooling flow in NGC 5044. We also obtained an upper for the spin temperature of $T_{\text{spin}} \leq 950$ K, suggesting that the observed H I is in the cold neutral phase.

ACKNOWLEDGMENTS

KR acknowledges the Smithsonian Combined Support for Life on a Sustainable Planet, Science, and Research administered by the Office of the Under Secretary for Science and Research. TD acknowledges funding from an NWO Rubicon Fellowship, project number 019.231EN.001. WF acknowledges support from the Smithsonian Institution, the Chandra High Resolution Camera Project through NASA contract NAS8-0306, NASA Grant 80NSSC19K0116, and Chandra Grant GO1-22132X. Basic research in radio astronomy at the U.S. Naval Research Laboratory is supported by 6.1 Base Funding. We acknowledge the use of the *ilifu* cloud computing facility - www.ilifu.ac.za, a partnership between the University of Cape Town, the University of the Western Cape, Stellenbosch University, Sol Plaatje University and the Cape Peninsula University of Technology. The *ilifu* facility is supported by contributions from the Inter-University Institute for Data Intensive Astronomy (IDIA - a partnership between the University of Cape Town, the University of Pretoria and the University of the Western Cape), the Computational Biology division at UCT and the Data Intensive Research Initiative of South Africa (DIRISA). This work made use of the CARTA (Cube Analysis and Rendering Tool for Astronomy) software. The authors thank the staff of the MeerKAT observatory for their help with the observations presented in this work. The MeerKAT telescope is operated by the South African Radio Astronomy Observatory, which is a facility of the National Research Foundation, an agency of the Department of Science and Innovation. We thank the staff of the GMRT that made these observations possible. GMRT is run by the National Centre for Radio Astrophysics of the Tata Institute of Fundamental Research.

Facilities: MeerKAT, uGMRT, CXO

Software: CARACal (Józsa et al. 2020), AOflagger (Ofringa et al. 2010), WSClean (Ofringa et al. 2014), SPAM (Intema et al. 2009), CARTA (Comrie et al. 2021), DS9 (Joye & Mandel 2003), SoFiA (Serra et al. 2015), SoFiA Image Pipeline, Astropy (Astropy Collaboration et al. 2013, 2018),

APLpy (Robitaille & Bressert 2012), Matplotlib (Hunter 2007)

APPENDIX

In Figure A.1, we present images of NGC 5044 obtained from archival GMRT data at 150 MHz (proposal code: 22_008), 235 MHz (proposal code: 17_034), and 610 MHz (proposal code: 17_034). Data reduction was carried out in SPAM. The overall morphology of the radio emission around NGC 5044 is consistent with that observed in our new deep wideband uGMRT and MeerKAT images. We emphasize that the noise levels in our archival GMRT images are comparable to those in previously published images. In Figure A.2, we present the highest-resolution MeerKAT L-band and VLA AnB configuration images (proposal code: 15A-243). The image is obtained by combining four BnA configuration data sets.

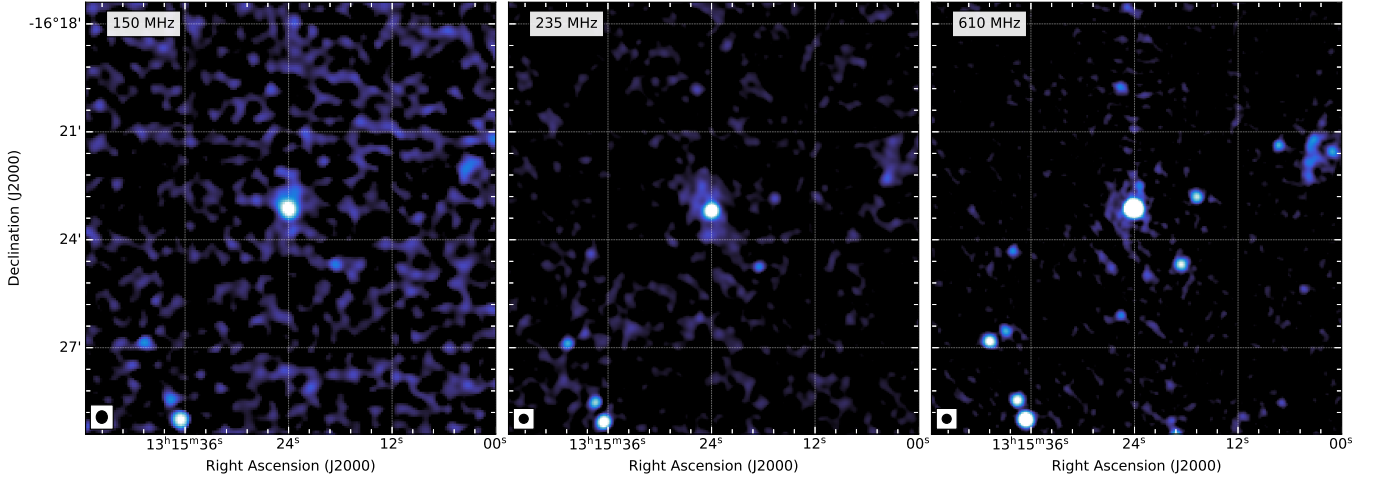


Figure A.1. GMRT archival 150 MHz ($20''$ resolution), 235 MHz ($15''$ resolution) and 610 MHz ($15''$ resolution) images. The noise level is 1 mJy beam^{-1} , $228 \mu\text{Jy beam}^{-1}$, $47 \mu\text{Jy beam}^{-1}$ at 150 MHz, 235 MHz, and 610 MHz, respectively. The beam size is indicated in the bottom left corner of the image.

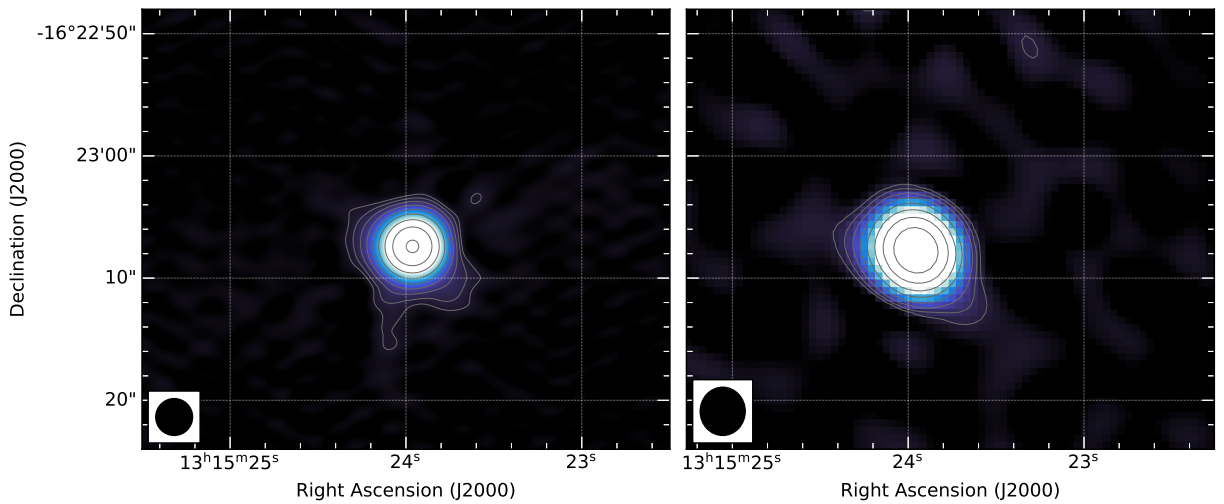


Figure A.2. High resolution VLA AnB configuration ($3''$) and MeerKAT 1.56 GHz ($3.9'' \times 3.7''$) images. The noise levels are $20 \mu\text{Jy beam}^{-1}$ and $23 \mu\text{Jy beam}^{-1}$ at 1.5 GHz and 1.28 GHz, respectively. The images are created using Briggs weighting with $\text{robust} = -2$ and an inner uv cut. Contours are drawn at $[1, 2, 4, 8, \dots] \times 5.0\sigma_{\text{rms}}$. The beam size is indicated in the bottom left corner of each image.

REFERENCES

- Allison, J. R. 2021, *Monthly Notices of the Royal Astronomical Society*, 503, 985, doi: [10.1093/mnras/stab518](https://doi.org/10.1093/mnras/stab518)
- Astropy Collaboration, Robitaille, T. P., Tollerud, E. J., et al. 2013, *A&A*, 558, A33, doi: [10.1051/0004-6361/201322068](https://doi.org/10.1051/0004-6361/201322068)
- Astropy Collaboration, Price-Whelan, A. M., Sipőcz, B. M., et al. 2018, *AJ*, 156, 123, doi: [10.3847/1538-3881/aabc4f](https://doi.org/10.3847/1538-3881/aabc4f)
- Bîrzan, L., McNamara, B. R., Nulsen, P. E. J., Carilli, C. L., & Wise, M. W. 2008, *ApJ*, 686, 859, doi: [10.1086/591416](https://doi.org/10.1086/591416)
- Bîrzan, L., Rafferty, D. A., Brüggen, M., et al. 2020, *MNRAS*, 496, 2613, doi: [10.1093/mnras/staa1594](https://doi.org/10.1093/mnras/staa1594)
- Boizelle, B. D., Walsh, J. L., Barth, A. J., et al. 2021, *ApJ*, 908, 19, doi: [10.3847/1538-4357/abd24d](https://doi.org/10.3847/1538-4357/abd24d)
- Bourne, M. A., & Sijacki, D. 2017, *MNRAS*, 472, 4707, doi: [10.1093/mnras/stx2269](https://doi.org/10.1093/mnras/stx2269)
- . 2021, *MNRAS*, 506, 488, doi: [10.1093/mnras/stab1662](https://doi.org/10.1093/mnras/stab1662)
- Brienza, M., Lovisari, L., Rajpurohit, K., et al. 2022, *A&A*, 661, A92, doi: [10.1051/0004-6361/202142579](https://doi.org/10.1051/0004-6361/202142579)
- Briggs, D. S. 1995, PhD thesis, New Mexico Institute of Mining and Technology
- Brunetti, G., & Jones, T. W. 2014, *International Journal of Modern Physics D*, 23, 1430007, doi: [10.1142/S0218271814300079](https://doi.org/10.1142/S0218271814300079)
- Brunetti, G., Setti, G., & Comastri, A. 1997, *A&A*, 325, 898, doi: [10.48550/arXiv.astro-ph/9704162](https://doi.org/10.48550/arXiv.astro-ph/9704162)
- Buote, D. A., Lewis, A. D., Brighenti, F., & Mathews, W. G. 2003, *ApJ*, 594, 741, doi: [10.1086/377094](https://doi.org/10.1086/377094)
- Churazov, E., Brüggen, M., Kaiser, C. R., Böhringer, H., & Forman, W. 2001, *ApJ*, 554, 261, doi: [10.1086/321357](https://doi.org/10.1086/321357)
- Churazov, E., Forman, W., Jones, C., & Böhringer, H. 2000, *A&A*, 356, 788, doi: [10.48550/arXiv.astro-ph/0002375](https://doi.org/10.48550/arXiv.astro-ph/0002375)
- Churazov, E., Sunyaev, R., Forman, W., & Böhringer, H. 2002, *MNRAS*, 332, 729, doi: [10.1046/j.1365-8711.2002.05332.x](https://doi.org/10.1046/j.1365-8711.2002.05332.x)
- Comrie, A., Wang, K.-S., Hsu, S.-C., et al. 2021, CARTA: The Cube Analysis and Rendering Tool for Astronomy, 2.0.0, Zenodo, doi: [10.5281/zenodo.4905459](https://doi.org/10.5281/zenodo.4905459)
- David, L. P., Jones, C., Forman, W., & Daines, S. 1994, *ApJ*, 428, 544, doi: [10.1086/174264](https://doi.org/10.1086/174264)
- David, L. P., Jones, C., Forman, W., et al. 2009, *ApJ*, 705, 624, doi: [10.1088/0004-637X/705/1/624](https://doi.org/10.1088/0004-637X/705/1/624)
- David, L. P., Vrtilek, J., O'Sullivan, E., et al. 2017, *ApJ*, 842, 84, doi: [10.3847/1538-4357/aa756c](https://doi.org/10.3847/1538-4357/aa756c)
- David, L. P., O'Sullivan, E., Jones, C., et al. 2011, *ApJ*, 728, 162, doi: [10.1088/0004-637X/728/2/162](https://doi.org/10.1088/0004-637X/728/2/162)
- David, L. P., Lim, J., Forman, W., et al. 2014, *ApJ*, 792, 94, doi: [10.1088/0004-637X/792/2/94](https://doi.org/10.1088/0004-637X/792/2/94)
- Davis, T. A., Greene, J. E., Ma, C.-P., et al. 2019, *MNRAS*, 486, 1404, doi: [10.1093/mnras/stz871](https://doi.org/10.1093/mnras/stz871)
- Deb, T., Verheijen, M. A. W., Poggianti, B. M., et al. 2022, *Monthly Notices of the Royal Astronomical Society*, 516, 2683–2696, doi: [10.1093/mnras/stac2441](https://doi.org/10.1093/mnras/stac2441)
- Desjardins, T. D., Gallagher, S. C., Hornschemeier, A. E., et al. 2014, *ApJ*, 790, 132
- Diniz, S. I. F., Pastoriza, M. G., Hernandez-Jimenez, J. A., et al. 2017, *MNRAS*, 470, 1703, doi: [10.1093/mnras/stx1322](https://doi.org/10.1093/mnras/stx1322)
- Donahue, M., & Voit, G. M. 2022, *PhR*, 973, 1, doi: [10.1016/j.physrep.2022.04.005](https://doi.org/10.1016/j.physrep.2022.04.005)
- Dong, R., Rasmussen, J., & Mulchaey, J. S. 2010, *ApJ*, 712, 883, doi: [10.1088/0004-637X/712/2/883](https://doi.org/10.1088/0004-637X/712/2/883)
- Dressel, L. L., Bania, T. M., & Davis, M. M. 1983, *ApJL*, 266, L97, doi: [10.1086/183986](https://doi.org/10.1086/183986)
- Eckert, D., Gaspari, M., Gastaldello, F., Le Brun, A. M. C., & O'Sullivan, E. 2021, *Universe*, 7, 142, doi: [10.3390/universe7050142](https://doi.org/10.3390/universe7050142)
- Eckert, D., Etori, S., Coupon, J., et al. 2016, *A&A*, 592, A12
- Edge, A. C. 2001, *MNRAS*, 328, 762, doi: [10.1046/j.1365-8711.2001.04802.x](https://doi.org/10.1046/j.1365-8711.2001.04802.x)
- Fabian, A. C. 2012, *ARA&A*, 50, 455, doi: [10.1146/annurev-astro-081811-125521](https://doi.org/10.1146/annurev-astro-081811-125521)
- Gaspari, M., Temi, P., & Brighenti, F. 2017, *MNRAS*, 466, 677, doi: [10.1093/mnras/stw3108](https://doi.org/10.1093/mnras/stw3108)
- Gaspari, M., Tombesi, F., & Cappi, M. 2020, *Nature Astronomy*, 4, 10, doi: [10.1038/s41550-019-0970-1](https://doi.org/10.1038/s41550-019-0970-1)
- Gastaldello, F., Buote, D. A., Humphrey, P. J., et al. 2007, *ApJ*, 669, 158, doi: [10.1086/521519](https://doi.org/10.1086/521519)
- Gastaldello, F., Buote, D. A., Temi, P., et al. 2009, *ApJ*, 693, 43, doi: [10.1088/0004-637X/693/1/43](https://doi.org/10.1088/0004-637X/693/1/43)
- Gastaldello, F., Di Gesu, L., Ghizzardi, S., et al. 2013, *ApJ*, 770, 56, doi: [10.1088/0004-637X/770/1/56](https://doi.org/10.1088/0004-637X/770/1/56)
- Giacintucci, S., Markevitch, M., Cassano, R., et al. 2019, *ApJ*, 880, 70, doi: [10.3847/1538-4357/ab29f1](https://doi.org/10.3847/1538-4357/ab29f1)
- Giacintucci, S., Vrtilek, J. M., O'Sullivan, E., et al. 2009, in *American Institute of Physics Conference Series*, Vol. 1201, The Monster's Fiery Breath: Feedback in Galaxies, Groups, and Clusters, ed. S. Heinz & E. Wilcots (AIP), 229–232, doi: [10.1063/1.3293043](https://doi.org/10.1063/1.3293043)
- Giacintucci, S., O'Sullivan, E., Vrtilek, J., et al. 2011, *ApJ*, 732, 95, doi: [10.1088/0004-637X/732/2/95](https://doi.org/10.1088/0004-637X/732/2/95)
- Giacintucci, S., O'Sullivan, E., Clarke, T. E., et al. 2012, *ApJ*, 755, 172, doi: [10.1088/0004-637X/755/2/172](https://doi.org/10.1088/0004-637X/755/2/172)
- Gitti, M., Brighenti, F., & McNamara, B. R. 2012, *Advances in Astronomy*, 2012, 950641, doi: [10.1155/2012/950641](https://doi.org/10.1155/2012/950641)
- Grossová, R., Werner, N., Massaro, F., et al. 2022, *ApJS*, 258, 30, doi: [10.3847/1538-4365/ac366c](https://doi.org/10.3847/1538-4365/ac366c)
- Healy, J., Deb, T., Verheijen, M. A. W., et al. 2021, *A&A*, 654, A173, doi: [10.1051/0004-6361/202141377](https://doi.org/10.1051/0004-6361/202141377)
- Hogan, M. T. 2014, PhD thesis, Durham University, UK
- Hunter, J. D. 2007, *Computing in Science & Engineering*, 9, 90, doi: [10.1109/MCSE.2007.55](https://doi.org/10.1109/MCSE.2007.55)

- Ignesti, A., Brunetti, G., Gitti, M., & Giacintucci, S. 2020, *A&A*, 640, A37, doi: [10.1051/0004-6361/201937207](https://doi.org/10.1051/0004-6361/201937207)
- Intema, H. T., van der Tol, S., Cotton, W. D., et al. 2009, *A&A*, 501, 1185, doi: [10.1051/0004-6361/200811094](https://doi.org/10.1051/0004-6361/200811094)
- Jaffe, W., & McNamara, B. R. 1994, *ApJ*, 434, 110, doi: [10.1086/174708](https://doi.org/10.1086/174708)
- Jaffe, W. J., & Perola, G. C. 1973, *A&A*, 26, 423
- Joye, W. A., & Mandel, E. 2003, in *Astronomical Society of the Pacific Conference Series*, Vol. 295, *Astronomical Data Analysis Software and Systems XII*, ed. H. E. Payne, R. I. Jedrzejewski, & R. N. Hook, 489
- Józsa, G. I. G., White, S. V., Thorat, K., et al. 2020, *CARACal: Containerized Automated Radio Astronomy Calibration pipeline*, *Astrophysics Source Code Library*, record ascl:2006.014. <http://ascl.net/2006.014>
- Kaneda, H., Onaka, T., Sakon, I., et al. 2008, *ApJ*, 684, 270, doi: [10.1086/590243](https://doi.org/10.1086/590243)
- Kenyon, J. S., Smirnov, O. M., Grobler, T. L., & Perkins, S. J. 2018, *MNRAS*, 478, 2399, doi: [10.1093/mnras/sty1221](https://doi.org/10.1093/mnras/sty1221)
- Kilborn, V. A., Forbes, D. A., Barnes, D. G., et al. 2009, *MNRAS*, 400, 1962
- Kirkpatrick, C. C., McNamara, B. R., & Cavagnolo, K. W. 2011, *ApJ*, 731, L23, doi: [10.1088/2041-8205/731/2/L23](https://doi.org/10.1088/2041-8205/731/2/L23)
- Kokotanekov, G., Wise, M., Heald, G. H., et al. 2017, *A&A*, 605, A48, doi: [10.1051/0004-6361/201730940](https://doi.org/10.1051/0004-6361/201730940)
- Kolokythas, K., O’Sullivan, E., Intema, H., et al. 2019, *MNRAS*, 489, 2488, doi: [10.1093/mnras/stz2082](https://doi.org/10.1093/mnras/stz2082)
- Kolokythas, K., O’Sullivan, E., Raychaudhury, S., et al. 2018, *MNRAS*, 481, 1550, doi: [10.1093/mnras/sty2030](https://doi.org/10.1093/mnras/sty2030)
- Lakhchaura, K., Werner, N., Sun, M., et al. 2018, *MNRAS*, 481, 4472, doi: [10.1093/mnras/sty2565](https://doi.org/10.1093/mnras/sty2565)
- Lovisari, L., Reiprich, T. H., & Schellenberger, G. 2015, *A&A*, 573, A118, doi: [10.1051/0004-6361/201423954](https://doi.org/10.1051/0004-6361/201423954)
- Maccagni, F. M., Ruffa, I., Loni, A., et al. 2023, *A&A*, 675, A59, doi: [10.1051/0004-6361/202346521](https://doi.org/10.1051/0004-6361/202346521)
- McNamara, B. R., & Nulsen, P. E. J. 2012, *New Journal of Physics*, 14, 055023, doi: [10.1088/1367-2630/14/5/055023](https://doi.org/10.1088/1367-2630/14/5/055023)
- Meyer, M., Robotham, A., Obreschkow, D., et al. 2017, *PASA*, 34, 52, doi: [10.1017/pasa.2017.31](https://doi.org/10.1017/pasa.2017.31)
- Morganti, R., & Oosterloo, T. 2018, *A&A Rv*, 26, 4, doi: [10.1007/s00159-018-0109-x](https://doi.org/10.1007/s00159-018-0109-x)
- Morganti, R., Peck, A. B., Oosterloo, T. A., et al. 2009, *A&A*, 505, 559, doi: [10.1051/0004-6361/200912605](https://doi.org/10.1051/0004-6361/200912605)
- Morganti, R., de Zeeuw, P. T., Oosterloo, T. A., et al. 2006, *MNRAS*, 371, 157, doi: [10.1111/j.1365-2966.2006.10681.x](https://doi.org/10.1111/j.1365-2966.2006.10681.x)
- Morsony, B. J., Heinz, S., Brüggén, M., & Ruszkowski, M. 2010, *MNRAS*, 407, 1277, doi: [10.1111/j.1365-2966.2010.17059.x](https://doi.org/10.1111/j.1365-2966.2010.17059.x)
- Murgia, M., Govoni, F., Markevitch, M., et al. 2009, *A&A*, 499, 679, doi: [10.1051/0004-6361/200911659](https://doi.org/10.1051/0004-6361/200911659)
- Obreschkow, D., & Rawlings, S. 2009, *MNRAS*, 394, 1857, doi: [10.1111/j.1365-2966.2009.14497.x](https://doi.org/10.1111/j.1365-2966.2009.14497.x)
- Odekon, M. C., Koopmann, R. A., Haynes, M. P., et al. 2016, *ApJ*, 824, 110
- Offringa, A. R., de Bruyn, A. G., Biehl, M., et al. 2010, *MNRAS*, 405, 155, doi: [10.1111/j.1365-2966.2010.16471.x](https://doi.org/10.1111/j.1365-2966.2010.16471.x)
- Offringa, A. R., McKinley, B., Hurley-Walker, N., et al. 2014, *MNRAS*, 444, 606, doi: [10.1093/mnras/stu1368](https://doi.org/10.1093/mnras/stu1368)
- Olivares, V., Salomé, P., Combes, F., et al. 2019, *A&A*, 631, A22, doi: [10.1051/0004-6361/201935350](https://doi.org/10.1051/0004-6361/201935350)
- Olivares, V., Salomé, P., Hamer, S. L., et al. 2022, *A&A*, 666, A94, doi: [10.1051/0004-6361/202142475](https://doi.org/10.1051/0004-6361/202142475)
- O’Sullivan, E., David, L. P., & Vrtilik, J. M. 2014, *MNRAS*, 437, 730, doi: [10.1093/mnras/stt1926](https://doi.org/10.1093/mnras/stt1926)
- O’Sullivan, E., Kolokythas, K., Kantharia, N. G., et al. 2018, *MNRAS*, 473, 5248, doi: [10.1093/mnras/stx2702](https://doi.org/10.1093/mnras/stx2702)
- O’Sullivan, E., Vrtilik, J. M., Harris, D. E., & Ponman, T. J. 2007, *ApJ*, 658, 299, doi: [10.1086/511778](https://doi.org/10.1086/511778)
- O’Sullivan, E., Worrall, D. M., Birkinshaw, M., et al. 2011, *MNRAS*, 416, 2916, doi: [10.1111/j.1365-2966.2011.19239.x](https://doi.org/10.1111/j.1365-2966.2011.19239.x)
- O’Sullivan, E., Ponman, T. J., Kolokythas, K., et al. 2017, *MNRAS*, 472, 1482, doi: [10.1093/mnras/stx2078](https://doi.org/10.1093/mnras/stx2078)
- O’Sullivan, E., Rajpurohit, K., Schellenberger, G., et al. 2024, *ApJ*, 970, 65, doi: [10.3847/1538-4357/ad4ed6](https://doi.org/10.3847/1538-4357/ad4ed6)
- Pasini, T., Finoguenov, A., Brüggén, M., et al. 2021, *MNRAS*, 505, 2628, doi: [10.1093/mnras/stab1451](https://doi.org/10.1093/mnras/stab1451)
- Pasini, T., Brüggén, M., Hoang, D. N., et al. 2022, *A&A*, 661, A13, doi: [10.1051/0004-6361/202141211](https://doi.org/10.1051/0004-6361/202141211)
- Plšek, T., Werner, N., Topinka, M., & Simionescu, A. 2024, *MNRAS*, 527, 3315, doi: [10.1093/mnras/stad3371](https://doi.org/10.1093/mnras/stad3371)
- Pulido, F. A., McNamara, B. R., Edge, A. C., et al. 2018, *ApJ*, 853, 177, doi: [10.3847/1538-4357/aaa54b](https://doi.org/10.3847/1538-4357/aaa54b)
- Randall, S. W., Nulsen, P. E. J., Jones, C., et al. 2015, *ApJ*, 805, 112, doi: [10.1088/0004-637X/805/2/112](https://doi.org/10.1088/0004-637X/805/2/112)
- Robitaille, T., & Bressert, E. 2012, *APLpy: Astronomical Plotting Library in Python*. <http://ascl.net/1208.017>
- Rose, T., Edge, A. C., Combes, F., et al. 2019, *MNRAS*, 489, 349, doi: [10.1093/mnras/stz2138](https://doi.org/10.1093/mnras/stz2138)
- Rose, T., McNamara, B. R., Combes, F., et al. 2023, *MNRAS*, 518, 878, doi: [10.1093/mnras/stac3194](https://doi.org/10.1093/mnras/stac3194)
- . 2024, *MNRAS*, 533, 771, doi: [10.1093/mnras/stae1831](https://doi.org/10.1093/mnras/stae1831)
- Ruffa, I., Prandoni, I., Laing, R. A., et al. 2019a, *MNRAS*, 484, 4239, doi: [10.1093/mnras/stz255](https://doi.org/10.1093/mnras/stz255)
- Ruffa, I., Davis, T. A., Prandoni, I., et al. 2019b, *MNRAS*, 489, 3739, doi: [10.1093/mnras/stz2368](https://doi.org/10.1093/mnras/stz2368)
- Russell, H. R., McNamara, B. R., Fabian, A. C., et al. 2019, *MNRAS*, 490, 3025, doi: [10.1093/mnras/stz2719](https://doi.org/10.1093/mnras/stz2719)
- Salomé, P., & Combes, F. 2003, *A&A*, 412, 657, doi: [10.1051/0004-6361:20031438](https://doi.org/10.1051/0004-6361:20031438)

- Sanders, J. S., Fabian, A. C., & Taylor, G. B. 2009, *MNRAS*, 396, 1449, doi: [10.1111/j.1365-2966.2009.14892.x](https://doi.org/10.1111/j.1365-2966.2009.14892.x)
- Saraf, M., Wong, O. I., Cortese, L., & Koribalski, B. S. 2023, *MNRAS*, 519, 4128, doi: [10.1093/mnras/stac3695](https://doi.org/10.1093/mnras/stac3695)
- Scaife, A. M. M., & Heald, G. H. 2012, *MNRAS*, 423, L30, doi: [10.1111/j.1745-3933.2012.01251.x](https://doi.org/10.1111/j.1745-3933.2012.01251.x)
- Schellenberger, G., David, L. P., Vrtilek, J., et al. 2021, *ApJ*, 906, 16, doi: [10.3847/1538-4357/abc488](https://doi.org/10.3847/1538-4357/abc488)
- . 2020, *ApJ*, 894, 72, doi: [10.3847/1538-4357/ab879c](https://doi.org/10.3847/1538-4357/ab879c)
- Schellenberger, G., O’Sullivan, E., David, L. P., et al. 2024, *ApJ*, 976, 246, doi: [10.3847/1538-4357/ad89bc](https://doi.org/10.3847/1538-4357/ad89bc)
- Serra, P., Oosterloo, T., Morganti, R., et al. 2012, *MNRAS*, 422, 1835, doi: [10.1111/j.1365-2966.2012.20219.x](https://doi.org/10.1111/j.1365-2966.2012.20219.x)
- Serra, P., Westmeier, T., Giese, N., et al. 2015, *MNRAS*, 448, 1922, doi: [10.1093/mnras/stv079](https://doi.org/10.1093/mnras/stv079)
- Temi, P., Amblard, A., Gitti, M., et al. 2018, *ApJ*, 858, 17, doi: [10.3847/1538-4357/aab9b0](https://doi.org/10.3847/1538-4357/aab9b0)
- Tonry, J. L., Dressler, A., Blakeslee, J. P., et al. 2001, *ApJ*, 546, 681, doi: [10.1086/318301](https://doi.org/10.1086/318301)
- Ubertosi, F., Gitti, M., Brighenti, F., et al. 2023, *ApJ*, 944, 216, doi: [10.3847/1538-4357/acacf9](https://doi.org/10.3847/1538-4357/acacf9)
- van Weeren, R. J., Timmerman, R., Vaidya, V., et al. 2024, *arXiv e-prints*, arXiv:2410.02863, doi: [10.48550/arXiv.2410.02863](https://doi.org/10.48550/arXiv.2410.02863)
- Vantyghem, A. N., McNamara, B. R., Edge, A. C., et al. 2017, *ApJ*, 848, 101, doi: [10.3847/1538-4357/aa8fd0](https://doi.org/10.3847/1538-4357/aa8fd0)
- Welch, G. A., Sage, L. J., & Young, L. M. 2010, *ApJ*, 725, 100, doi: [10.1088/0004-637X/725/1/100](https://doi.org/10.1088/0004-637X/725/1/100)
- Werner, N., Oonk, J. B. R., Sun, M., et al. 2014, *MNRAS*, 439, 2291, doi: [10.1093/mnras/stu006](https://doi.org/10.1093/mnras/stu006)
- Wolfire, M. G., Hollenbach, D., McKee, C. F., Tielens, A. G. G. M., & Bakes, E. L. O. 1995, *ApJ*, 443, 152, doi: [10.1086/175510](https://doi.org/10.1086/175510)
- Young, L. M., Bureau, M., Davis, T. A., et al. 2011, *MNRAS*, 414, 940, doi: [10.1111/j.1365-2966.2011.18561.x](https://doi.org/10.1111/j.1365-2966.2011.18561.x)